Article:

Malatesta, L.C. orcid.org/0000-0003-0983-715X, Avouac, J.-P., Brown, N.D. et al. (9 more authors) (2018) Lag and mixing during sediment transfer across the Tian Shan piedmont caused by climate-driven aggradation-incision cycles. Basin Research, 30 (4). pp. 613-635. ISSN 0950-091X

https://doi.org/10.1111/bre.12267

Lag and mixing during sediment transfer across the Tian Shan piedmont caused by climate-driven aggradation–incision cycles

Luca C. Malatesta,*,† Jean-Philippe Avouac,* Nathan D. Brown,‡ Sebastian F. M. Breitenbach,§ Jiawei Pan,¶ Marie-Luce Chevalier,¶ Edward Rhodes,‡,** Dimitri Saint-Carlier,†† Wenjing Zhang,¶ Julien Charreau,†† Jérôme Lavé†† and Pierre-Henri Blard††

*Division of Geological and Planetary Sciences, California Institute of Technology, Pasadena, CA, USA
†Department of Earth and Planetary Sciences, University of California Santa Cruz, Santa Cruz, CA, USA
‡Department of Earth, Planetary, and Space Sciences, University of California, Los Angeles, CA, USA
§Institute of Geology, Mineralogy and Geophysics, Ruhr-Universität Bochum, Bochum, Germany
¶Institute of Geology, Chinese Academy of Geological Sciences, Beijing, China
**Department of Geography, The University of Sheffield, Sheffield, UK
††Centre de Recherches Pétrographiques et Géochimiques, Vandoeuvre-lès-Nancy, France

ABSTRACT

Transient sediment storage and mixing of deposits of various ages during transport across alluvial piedmonts alter the clastic sedimentary record. We quantify buffering and mixing during cycles of aggradation–incision in the north piedmont of the Eastern Tian Shan. We complement existing chronologic data with 20 new luminescence ages and one cosmogenic radionuclide age of terrace abandonment and alluvial aggradation. Over the last 0.5 Myr, the piedmont deeply incised and aggraded many times per 100 kyr. Aggradation is driven by an increased flux of glacial sediment accumulated in the high range and flushed onto the piedmont by greater water discharge at stadial–interstadial transitions. After this sediment is evacuated from the high range, the reduced input sediment flux results in fluvial incision of the piedmont as fast as 9 cm year^{-1} and to depths up to 330 m. The timing of incision onset is different in each river and does not directly reflect climate forcing but the necessary time for the evacuation of glacial sediment from the high range. A significant fraction of sediments evacuated from the high range is temporarily stored on the piedmont before a later incision phase delivers it to the basin. Coarse sediments arrive in the basin with a lag of at least 7–14 kyrs between the first evacuation from the mountain and later basinward transport. The modern output flux of coarse sediments from the piedmont contains a significant amount of recycled material that was deposited on the piedmont as early as the Middle Pleistocene. Variations in temperature and moisture delivered by the Westerlies are the likely cause of repeated aggradation–incision cycles in the north piedmont instead of monsoonal precipitation. The arrival of the gravel front into the proximal basin is delayed relative to the fine-grained load and both are separated by a hiatus. This work shows, based on field observations and data, how sedimentary systems respond to climatic perturbations, and how sediment recycling and mixing can ensue.

INTRODUCTION

Most mountain ranges on Earth are bounded by alluvial piedmonts. The piedmonts can temporarily trap part of the sediment flux through episodes of aggradation and subsequent incision, controlling the spatial and temporal delivery of sediments from the bedrock source to the foreland basin sink (e.g. Paola *et al.*, 1992; Métivier, 2002; Allen, 2008; Allen *et al.*, 2013). The sedimentary outflux from piedmont to basin is a mixture of fresh input from the mountain and of recycled older piedmont deposits, the ratio of which depends on the pattern and timing of alluvial aggradation and incision. The degree of mixing and buffering of the sediment flux affects the preservation of the environmental signals it carries (Allen, 1997;

Correspondence: Luca C. Malatesta, Department of Earth and Planetary Sciences, University of California Santa Cruz, 1156 High St., Santa Cruz, CA 95064 USA. E-mail: lcmalate@ucsc.edu

Romans *et al.*, 2015). The effect of aggradation–incision cycles on the sediment routing system is poorly known. How rapid and how large are these cycles? And how do they relate to climatic and tectonic forcing?

Alluvial piedmonts are built by transport-limited rivers – from wide sheet flow to narrow entrenched channels (Bull, 1977; Parker *et al.*, 1998a,b; Nicholas & Quine, 2007; Pepin *et al.*, 2010) – that distribute the coarse sediment load on alluvial fans and primarily react to changes in the fluxes of water and sediment. Alluvial slopes scale inversely with water discharge (Gilbert & Murphy, 1914; Mackin, 1948; Hooke, 1968), and positively with the ratio of sediment flux over water discharge Q_s/Q_w (Schumm, 1973; Leopold & Bull, 1979). This makes alluvial fans particularly sensitive to climatic forcing (Bull, 1991; Molnar *et al.*, 1994; Tucker & Slingerland, 1997; Rohais *et al.*, 2012; D'Arcy & Whittaker, 2014). Alluvial piedmonts are relatively steep and the rivers crossing them deliver their suspended and dissolved load directly to the basin, whereas the bedload of the piedmont rivers, coarse sand to cobbles, builds the bulk of the fan morphology (Paola *et al.*, 1992; Smith & Ferguson, 1996; Allen *et al.*, 2013). However, the bedload is only a fraction of the total (solid and dissolved) sediment flux of a river. The bedload fraction tends to decrease downriver and amounts to 30%–50% of the solid load in sand bedded streams (Turowski *et al.*, 2010). Along the Eastern Tian Shan river Urumqi, ~20% of the total load is transported as bedload in the high range (Liu *et al.*, 2011).

To address questions related to the intricate links between tectonics, climate, hydrology and geomorphology, we investigate the northern piedmont of the Eastern Tian Shan. The piedmont is formed by alluvial fans which have coalesced in a bajada and are deformed in a fold-and-thrust belt (Avouac *et al.*, 1993). The Late Pleistocene fans of the north piedmont have been deeply incised in the Holocene and provide an excellent opportunity to study a reasonably simple system. River incision is linked to changes in temperature and moisture carried by the summer monsoon and/or Westerlies (Poisson & Avouac, 2004). We present the field area in the Section Geological Setting of the North Piedmont of the Eastern Tian Shan and describe the study sites in the Section Geometry of Alluvial terraces and Sediment Characteristics. We then present new luminescence ages that constrain the chronology of terrace abandonment and stratigraphic accumulation in the Section Chronological Constraints. This new data set is combined with previously published age constraints in the Section Morphological Evolution of the Piedmont. In the Section Pleistocene Climate and Aggradation–Incision Cycles, we compare our observations with the record of Central Asian climate in the Pleistocene and show that variations in the Westerlies are the main driver of aggradation–incision cycles. Finally, we discuss the stratigraphic consequences of the temporary storage of sediment during these aggradation–incision cycles in piedmonts.

GEOLOGICAL SETTING OF THE NORTH PIEDMONT OF THE EASTERN TIAN SHAN

The Tian Shan range was initially formed around two late Palaeozoic sutures (Windley *et al.*, 1990). Throughout the Mesozoic and early Cenozoic, a reduction in mountain relief and occasional reactivations of the range are documented by thermochronology and sediment fluxes into the adjacent basins: Tarim to the south and Junggar to the north (Windley *et al.*, 1990; Hendrix *et al.*, 1992; Métivier & Gaudemer, 1999; Dumitru *et al.*, 2001; Jolivet *et al.*, 2013). At *ca.* 24 Ma, the India-Eurasia collision reactivated Central Asian structures and mountain building along the Tian Shan Palaeozoic suture by rigid block rotation north of the Himalayas (Avouac & Tapponnier, 1993; Sobel & Dumitru, 1997). Large volumes of Oligocene coarse clastic material deposited atop an unconformity in the Tarim and Junggar Basins document the renewed mountain building that ensued (Windley *et al.*, 1990; Métivier & Gaudemer, 1997). North–south compression resulted in the development of dominant east-striking reverse faults and large southeast-striking right-lateral strike-slip faults (Tapponnier & Molnar, 1979). Shortening is distributed across the southern and northern fold-and-thrust belts that were activated at *ca.* 24 Ma (Hendrix *et al.*, 1994; Dumitru *et al.*, 2001) and within the deforming inner mountain basins (Thompson *et al.*, 2002; Fu *et al.*, 2003; Jolivet *et al.*, 2010; Saint-Carlier *et al.*, 2016). Along the northern piedmont (Fig. 1), several parallel rows of east–southeast-striking anticlines deform foreland sediments and absorb about 3 mm year^{-1} of shortening (Avouac *et al.*, 1993; Molnar *et al.*, 1994; Burchfiel *et al.*, 1999; Stockmeyer *et al.*, 2017). Structural sections and seismic profiles suggest that the thrust faults in the piedmont splay from a single detachment, characterised by ramps and flats, which roots southwards beneath the high range (Avouac *et al.*, 1993; Burchfiel *et al.*, 1999; Wang *et al.*, 2004; Dengfa *et al.*, 2005; Stockmeyer *et al.*, 2014; Guan *et al.*, 2016).

The piedmont deposits that separate the basin from the high range consist of Jurassic to modern clastic sediment forming a *ca.* 50-km wide fold-and-thrust belt covered by a bajada of Quaternary alluvium (Fig. 1, Avouac *et al.*, 1993; Lu *et al.*, 2010b). The total relief of the piedmont is on the order of 800–1000 m over a distance of 25–45 km. Magnetostratigraphic studies show that local rates of sediment accumulation have been relatively steady at about 0.2 mm year^{-1} over the last 10 Myr (Charreau *et al.*, 2005, 2009; Lu *et al.*, 2010b, 2013). The erosion rate in

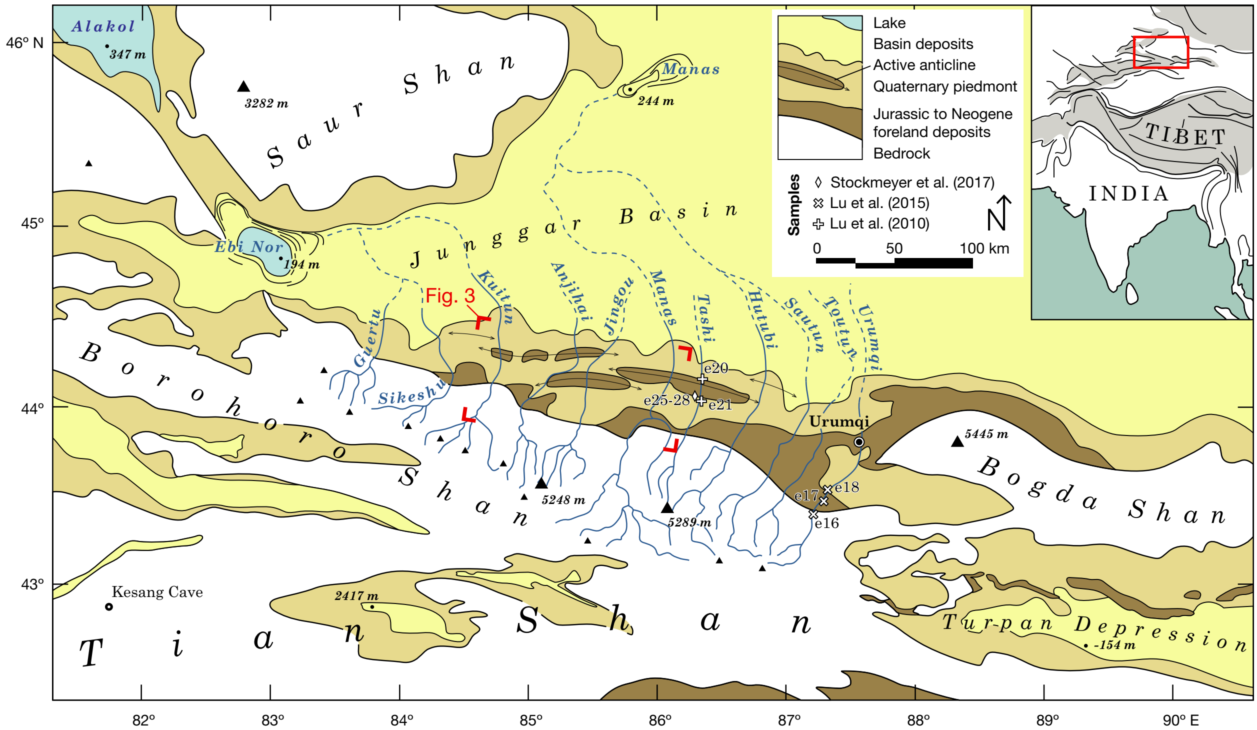

Fig. 1. Location map of the foreland and basin deposits and main rivers on the north side of the Eastern Tian Shan. The lakes Ebi Nor and Manas (dry) are the low points of the endorheic Junggar Basin. The sample labels (e#) refer to the compilation list of Table S3 in Appendix S1.

the high range has been estimated to be between 0.1 and 1 mm year^{-1} in the last 9 Myr with an excursion to 2–2.5 mm year^{-1} at the onset of Quaternary glaciations according to cosmogenic isotope measurements in exposed piedmont deposits (Charreau *et al.*, 2011; Puchol *et al.*, 2016). Guerit *et al.* (2016) estimated erosion rates of around 0.135 mm year^{-1} for the last 300 kyr from the mass balance of 10 alluvial fans in the northern piedmont of the Eastern Tian Shan. Guerit *et al.* (2016) also suggested that the dry Central Asian climate of the last few million years is responsible for the imbalance between these very low erosion rates and the comparatively large shortening rates of 10 ± 3 mm year^{-1} (Reigber *et al.*, 2001).

East of the Kuitun River, most of the rivers first cross folded and thrusted Jurassic to Neogene foreland deposits before reaching the Pleistocene series. The deformation front defined by the Dushanzi, Huergosi, Manas and Tugulu anticlines exposes Paleogene to Pleistocene foreland deposits that are actively eroding. After leaving the mountain and before entering the alluvial piedmont, the rivers east of the Anjihai River cross a wider swath of deformed and largely bevelled Jurassic to Neogene foreland deposits (Avouac *et al.*, 1993; Li *et al.*, 2010).

The main rivers flowing northwards out of the range have incised the piedmont by more than 100 m since the last deglaciation (20–15 ka) and older prominent terraces, uplifted by the anticlines, suggest that episodes of aggradation and incision occurred repeatedly (Molnar *et al.*, 1994). These authors proposed that the prominent terraces mark episodes of fluvial incision every 100 kyr during interglacial periods whereas aggradation occurs during glacial periods. The evolution of the piedmont rivers is driven by the periodic evacuation of large volumes of glacial and periglacial sediment from the glaciated upper half of the catchments (Stroeven *et al.*, 2013) where they accumulate during the stadials: first, the rivers building the alluvial fans aggrade and steepen under the increased sediment flux. Then, they quickly and deeply incise after the upstream reservoir is depleted, causing sediment-starved water to flow on, and erode, the over-steepened piedmont (Poisson & Avouac, 2004). The Holocene incision rates of 10–30 mm year^{-1} are one order of magnitude faster than the uplift of anticlines in the fold-and-thrust belt (Molnar *et al.*, 1994; Poisson & Avouac, 2004; Lu *et al.*, 2010a; Gong *et al.*, 2014). Holocene incision is interpreted to have resulted from hydrological changes induced by climate change, possibly summer monsoon incursions in Central Asia (Poisson & Avouac, 2004). An autogenic positive feedback between incision and valley morphology further enhances it: increasingly high valley walls force the river to flow in a narrower channel and promote downcutting (Malatesta *et al.*, 2017). Holocene incision and significant narrowing of the active floodplain carved several Holocene terraces that provide a detailed entrenchment history (e.g. 10

along the Kuitun River and 18 along the neighbouring Anjihai River, Fig. 2). The gravel previously deposited at the range front is now remobilised by incision and transported farther downstream, feeding the lower fans, located about 30-km downstream from the range front (Fig. 3, see also Jolivet *et al.*, 2014; Guerit *et al.*, 2016).

GEOMETRY OF ALLUVIAL TERRACES AND SEDIMENT CHARACTERISTICS

Our study focuses on four neighbouring rivers: Kuitun, Anjihai, Jingou and Manas (Fig. 3). Like all rivers of the north piedmont, they are characterised by wide fill terraces (2–3 km) incised by deep canyons at the bottom of which braided rivers flow in narrow floodplains (100's m). The fill-cut terraces of the alluvial fill become strath terraces as they cross anticlines and bedrock benches. Both types record the same incisional event and the discrimination between them is irrelevant here. Morphological similarities alone suggest a synchronised Holocene incision of all the rivers. As the Kuitun River crosses the Dushanzi anticline, a migrating bend of the locally narrowed channel abandoned a series of nine Holocene terraces (Figs 4 and 5). A flight of 19 terraces is preserved where the Toudao River flows into the Anjihai River

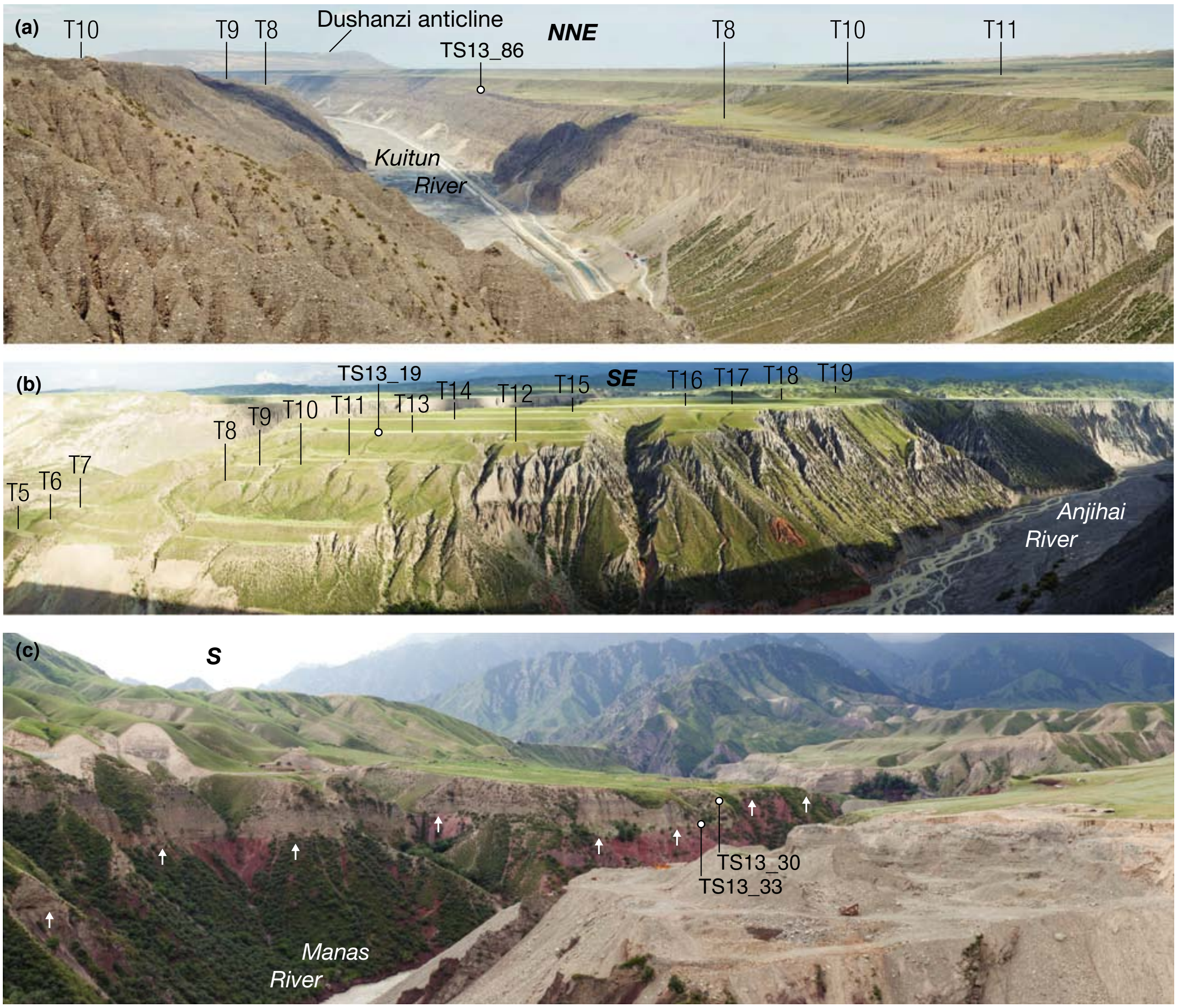

Fig. 2. Field pictures of the piedmont rivers, see Fig. 3 for location of the point of view. (a) Kuitun River, picture from the left wall at the apex looking north, where local incision is 330 m. The Dushanzi anticline is visible in the background. (b) Terrace flight along the Anjihai, looking to the southeast with the high range visible on the right. The river flows from right to left and is incised 240 m in Pleistocene conglomerate (grey and beige) and in tilted Neogene clastic series (red and rust). (c) Strath terraces of the upper Manas River looking south, the tilted Jurassic series is red. In the foreground, a gravel pit illustrates the thickness of the alluvial fill above the strath. The different levels of the strath are visible along the cliff (white arrows).

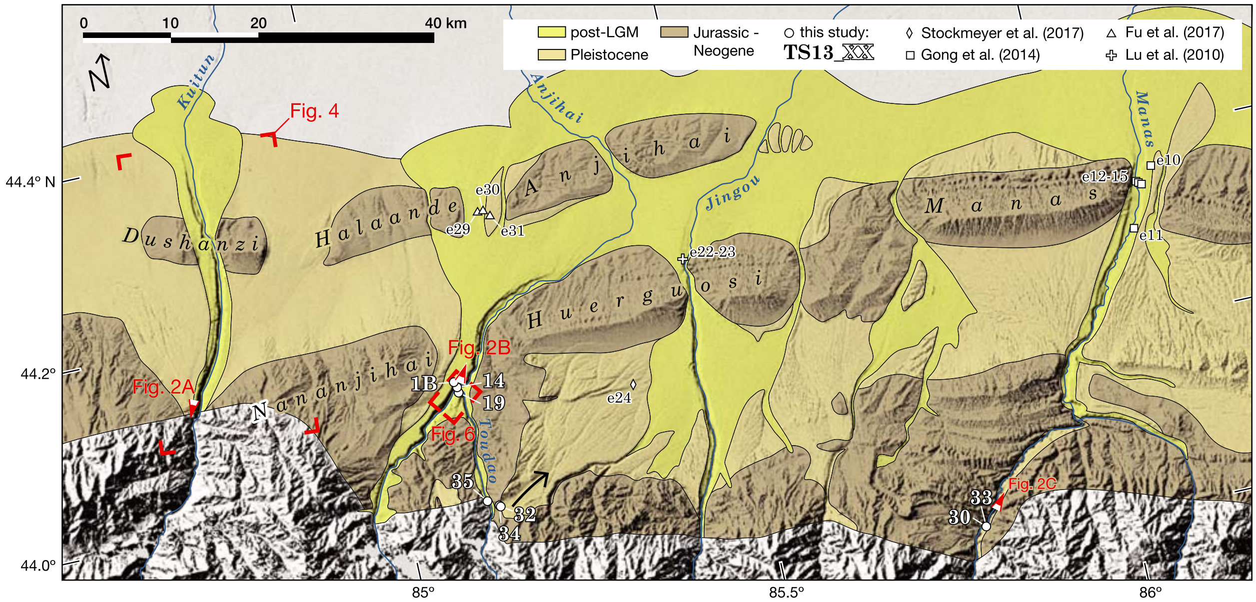

Fig. 3. Map of the north piedmont of the Eastern Tian Shan from the Kuitun to the Manas Rivers. Hillshade and elevation from ASTER GDEM v2 (a product of NASA and METI). Samples from this study are marked by two characters in white (last two characters from their field codes, see Table 1). The black sample labels starting with 'e' are from third party authors (Table S3 in Appendix S1). Samples for the Kuitun River are shown in Figs 4 and 7.

immediately upstream of the Huerguosi anticline (Figs 2, 3, and 6). The Manas River leaves the high range to traverse steeply dipping Jurassic and Cretaceous foreland deposits on which a wide strath is carved (Figs 2 and 3).

We used remote sensing data and field observations to map the various terraces in the study area. High-resolution satellite imagery came from Landsat, Digital Globe and Spot and is freely available on Google Earth and Bing Maps. The topographic data from ASTER GDEM2 (NASA and METI) and SRTM 1 arc second (NASA, USGS, DLR, ASI, NGIA) provide a good regional data set for the north piedmont of the Chinese Tian Shan. To compensate for insufficient resolution at the scale of individual terraces, we surveyed two terrace flights along the Kuitun and the Anjihai Rivers at very high resolution with a terrestrial LiDAR scanner (RIEGL VZ1000 Laser Measurement Systems, Austria) during a field expedition in May and June 2013. The LiDAR instrument is managed by the Key Laboratory of Continental Tectonics and Dynamics, Institute of Geology of the Chinese Academy of Geological Sciences in Beijing. Two areas were surveyed: seven point clouds cover the Kuitun River terrace series in the heart of the anticline and resolve nine Holocene terraces (Fig. 5); five point clouds cover a terrace series along the Anjihai River where 19 terraces document river incision (18 are captured at high resolution by the LiDAR survey, Fig. 6). The point clouds cover a radius of 1.2 km each and are subsampled at 0.5 m. We assembled them using the open source software *Cloud Compare* (version 2.7, GPL software, 2016, retrieved from http://www.cloudcompare.org) and analysed them with the software *Quick Terrain Modeler* from *Applied Imagery*.

Along the Kuitun River, we surveyed the distribution of grain sizes with areal sampling (Wolman, 1954) in the river bed (six sites, Figs 4 and 7) as well as in a steep and short tributary canyon (Swallows' Canyon) of the Kuitun River representing the valley walls (two sites, Fig. 7) in May and June 2013. Sampling method and results are described in Appendix S1 (Section 4 and Fig. S2). Swallows' Canyon offer exposures normal to the stream direction but without reliably identifiable cross-cutting relationships in the stratigraphy. The six surveys along the Kuitun River reveal a quick decrease in the 84th percentile (D_{84}) past the apex of the fan from 87 and 119 mm to *ca.* 50 mm (Fig. S2 in Appendix S1). Meanwhile the median grain size D_{50} remains constant along 30 km of the river with a mean value of 30.5 mm. The two samples in the tributary Swallows' Canyon have a D_{50} of 38 and 39 mm, with D_{84} of 70 and 78 mm.

CHRONOLOGICAL CONSTRAINTS

We compiled all the chronological constraints available from the literature (Poisson, 2002; Poisson & Avouac, 2004; Lu *et al.*, 2010a, 2014; Gong *et al.*, 2014; Stockmeyer *et al.*, 2017) and complemented them with our own data based on luminescence dating. Location and results for the new samples are listed in Table 1 and detailed descriptions of the sampling sites and the

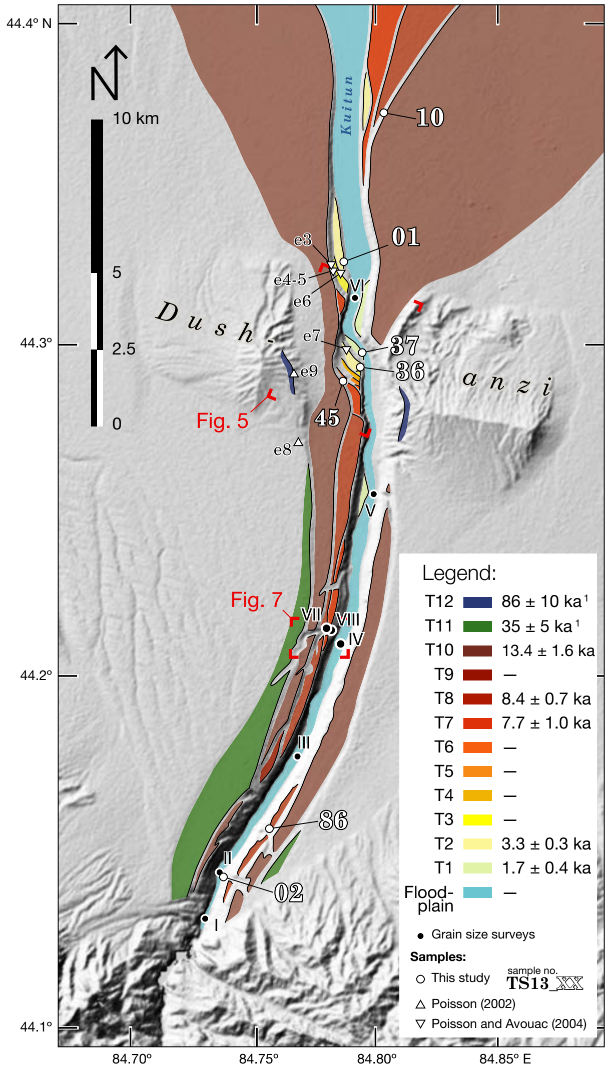

Fig. 4. Map of the Kuitun River flowing across its alluvial fan and location of samples (XX and e#) and grain size surveys (I to VI). Hillshade from SRTM v2 data. Third party samples: (1) Poisson & Avouac (2004); (2) Poisson (2002).

luminescence results are given in Appendix S1. The locations of the complete data set assembled for this study are indicated in Figs 1, 3, 4, and 7 and in Table S4 of Appendix S1.

Luminescence dating

Sampling approach

We sampled material for post-IR infrared stimulated luminescence (post-IR IRSL) dating (Huntley *et al.*, 1985; Aitken, 1998; Rhodes, 2011) to constrain (1) the timing of terrace abandonment by sampling the loess cover and/or the topmost alluvial deposits of terrace treads and (2) the timing of aggradation by sampling in the fan stratigraphy. The data set consists of seven samples for post-IR IRSL dates constraining terrace abandonment ages and 13 post-IR IRSL dates documenting alluvial aggradation ages. The samples were collected on terraces and within the banks of the Kuitun, Anjihai, and Manas Rivers. The alluvial fans are mostly built by gravels to cobbles and the fine-grained material necessary for post-IR IRSL measurement is scarce. We targeted silt to sand lenses deeper than ~30 cm and thicker than ~5 cm to be sampled with an aluminium tube. The loess samples are the simplest to obtain by hammering the tube into the base of the horizon, immediately above the top gravel of the alluvial fill. The loess deposition ages provide a minimum abandonment age for the respective terrace. This arid region is poor in organic material and no charcoal or other organic material was found for radiocarbon dating. Detailed descriptions of the sample settings and analytical results can be found in Appendix S1.

Equivalent dose determination

The preparation and measurement of the samples followed standard procedures for single-grain post-IR IRSL dating which are described in detail in Appendix S1. However, the equivalent dose values for some older fluvial samples cannot be interpreted using standard approaches because of the between-grain scatter. We develop a framework presented in detail hereafter to interpret such samples.

We use a single-grain post-IR IRSL method to determine the equivalent dose (D_e) since deposition. This technique has only recently been developed (Buylaert *et al.*, 2009; Thiel *et al.*, 2011), and few studies have applied the technique to single grains within fluvial deposits (Nian *et al.*, 2012; Trauerstein *et al.*, 2014; Brown *et al.*, 2015). This study explores the applicability of this method in a region where the quartz content has been measured to be as low as 0.05%–1% by weight.

With the exception of sample J0649, all measured samples yielded at least five single-grain results, with an average of 57 ± 33 grains out of 200 measured responding per sample. The distributions of D_e values fall into three categories: Types A, B, and C. Type A samples exhibited the simplest but least-common distribution: a single, well-bleached population, adequately described using the Central Age Model of Galbraith *et al.* (1999). Three samples fell into this category (see the 'Distribution type' column within Table S2 in Appendix S1). The other two distribution types exhibited an overdispersion parameter greater than what would be expected from a well-bleached population (well-bleached samples exhibit an overdispersion of about 20 ± 9% for multi-grain quartz OSL (optically stimulated luminescence), though variability is high and the parameter should be quantified for a given site; Arnold & Roberts, 2009). This situation arises when multiple dose populations are mixed together (e.g. bank

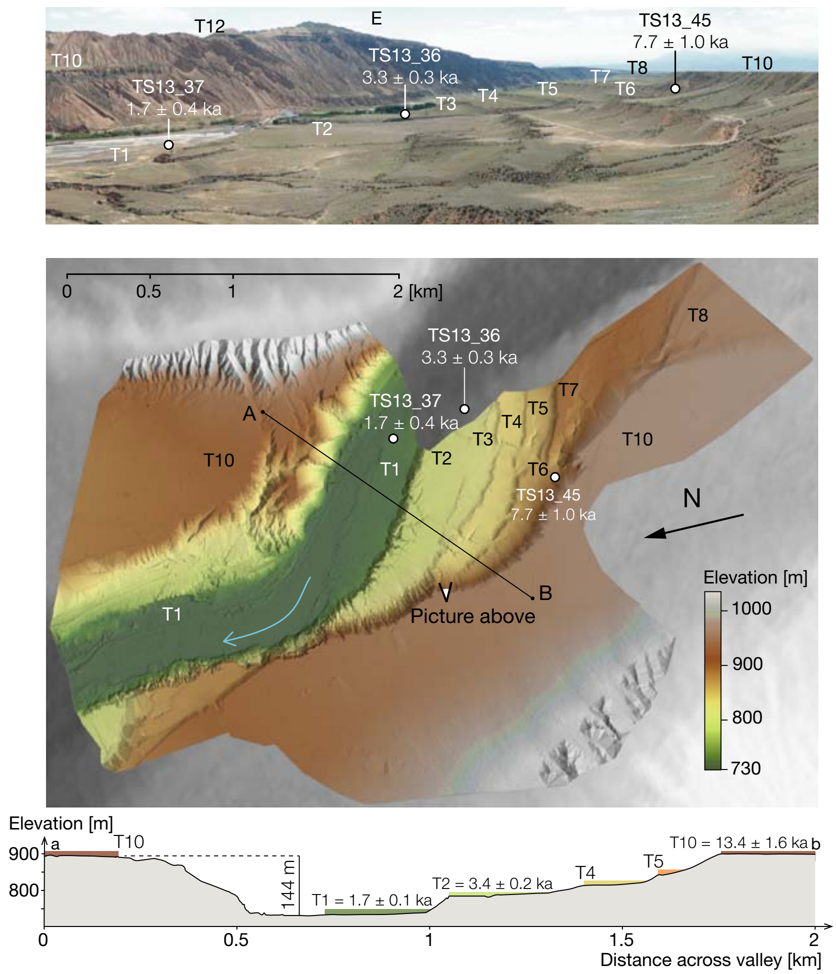

Fig. 5. Terrace flight of the Kuitun River in the Dushanzi anticline. Top: photo taken looking east-southeast, with the Kuitun River flowing from right to left, the oldest dated terrace uplifted by the anticline (T12) is visible in the background. The high range lies to the right. Centre: terrestrial LiDAR map of the terrace flight. Bottom: profile across the valley from the LiDAR data.

collapse during fluvial transport, bioturbation), when a sediment is not exposed to sunlight for a long enough time (i.e. partial bleaching) or due to problematic luminescence responses (thermal transfer, first-cycle sensitivity changes) (Neudorf *et al.*, 2012).

Of those distributions with high overdispersion, two types of D_e distributions were found. In Type B samples (12 of the 22 samples), the D_e values varied as a function of grain brightness and by considering only the brightest grains, the overdispersion could be reduced to reasonable values. This effect is shown for sample J0654 in Fig. 8a, b. To determine the D_e values for Type B samples, the brightest subset of grains were chosen to minimise the overdispersion, and then the Central Age Model (Galbraith *et al.*, 1999) was applied.

While the reason for this relationship between grain sensitivity and overdispersion is unknown, it seems that the variation in internal potassium content between grains is the likely reason. Smedley *et al.* (2012) have recently demonstrated the exponential increase of feldspar grain brightness as a function of K-content and Reimann *et al.* (2012) have shown that the brightest subset (e.g. 30%) of individual K-feldspar grains gives post-IR IRSL ages concordant with independent age controls. This is borne out in the only Type B sample with radiocarbon age controls, J0646, which has a post-IR IRSL age of 3.3 ± 0.3 ka, indistinguishable from ^{14}C samples C-T5-1 (3.33 ± 0.04 kyr BP) and C-T5-2 (3.4 ± 0.2 kyr BP) (Poisson & Avouac, 2004; Table S4 in Appendix S1).

Type C samples (5 of 22) retained high overdispersion even when only the brightest grains were considered. The source of inter-grain variability was therefore considered to reflect incomplete bleaching. Two routines were used to evaluate Type C D_e values. The Minimum Age Model (three variables, MAM-3; Galbraith *et al.*, 1999) was used, assuming an overdispersion of 25% (an average value from Type A and B samples). A Discrete Minimum Model (DMM) was also used (Fuchs & Lang, 2001; Rhodes, 2015) wherein first dim grains and then older grains were rejected until an overdispersion threshold of

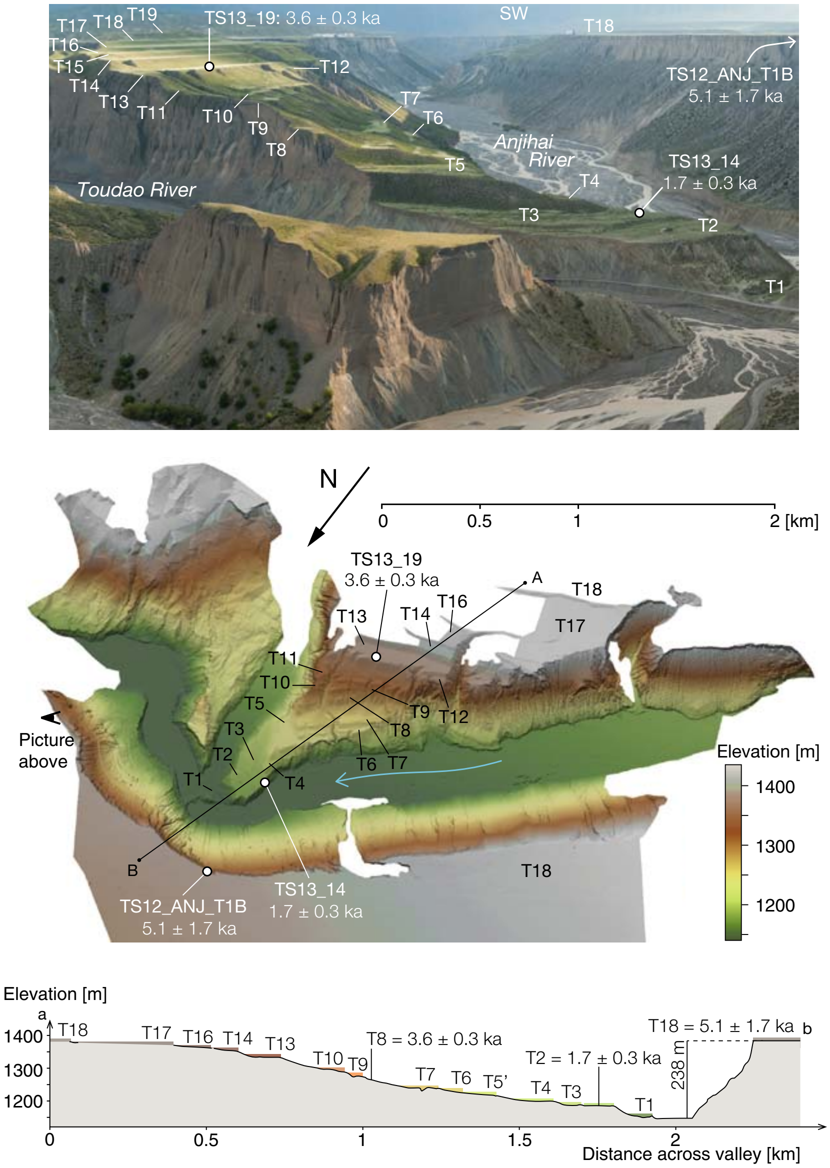

Fig. 6. Terrace flight of the Anjihai River at the junction with its tributary the Toudao River. Top: photo taken looking southwest, the Anjihai River is on the right and flows toward the camera, the Toudao River flows from the left. Tilted Neogene series (grey) outcrop at the base of the conglomerate cliff (brown). Centre: terrestrial LiDAR map of the terrace flight. Bottom: profile across the valley from the LiDAR data.

25% was reached. The results from these methods compare well, in most cases overlapping at 1 σ (Fig. S1 in Appendix S1).

Cosmogenic radionuclide dating

We infer the ages of abandonment of the terrace T18 along the Anjihai river from a depth distribution of cosmogenic isotope concentrations (Gosse & Phillips, 2001; Dunai, 2010). We sampled three granite cobbles from the surface and collected four samples of sand and small pebbles at different depths in a fresh open gravel quarry (Fig. S26 in Appendix S1). To invert the depth profile, we modified the formulation of Lal (1991) that describes the change in ^{10}Be concentration as a function of depth to account for the deposition of loess and/or soil after the terrace abandonment (Braucher *et al.*, 2011; Guralnik *et al.*, 2011). The exposure age was then derived from a Monte Carlo inversion procedure (Braucher *et al.*, 2009; Hidy *et al.*, 2010; Saint-Carlier *et al.*, 2016). The detail of the methods, the associated parameters and the sample treatment and analyses are provided in the online repository. Results of the cosmogenic analyses are reported in Table S2 (Appendix S1) of the online repository. The cosmogenic depth profile shows the expected exponential decrease below the loess horizon and its inversion constrains the mean exposure time of the terraces to 5.1 ± 1.7 ka (Fig. S27 in Appendix S1).

Results for the Kuitun River

Sampling in the Kuitun River followed two objectives: complementing the published data set of Holocene terrace abandonment ages (Poisson, 2002; Poisson & Avouac,

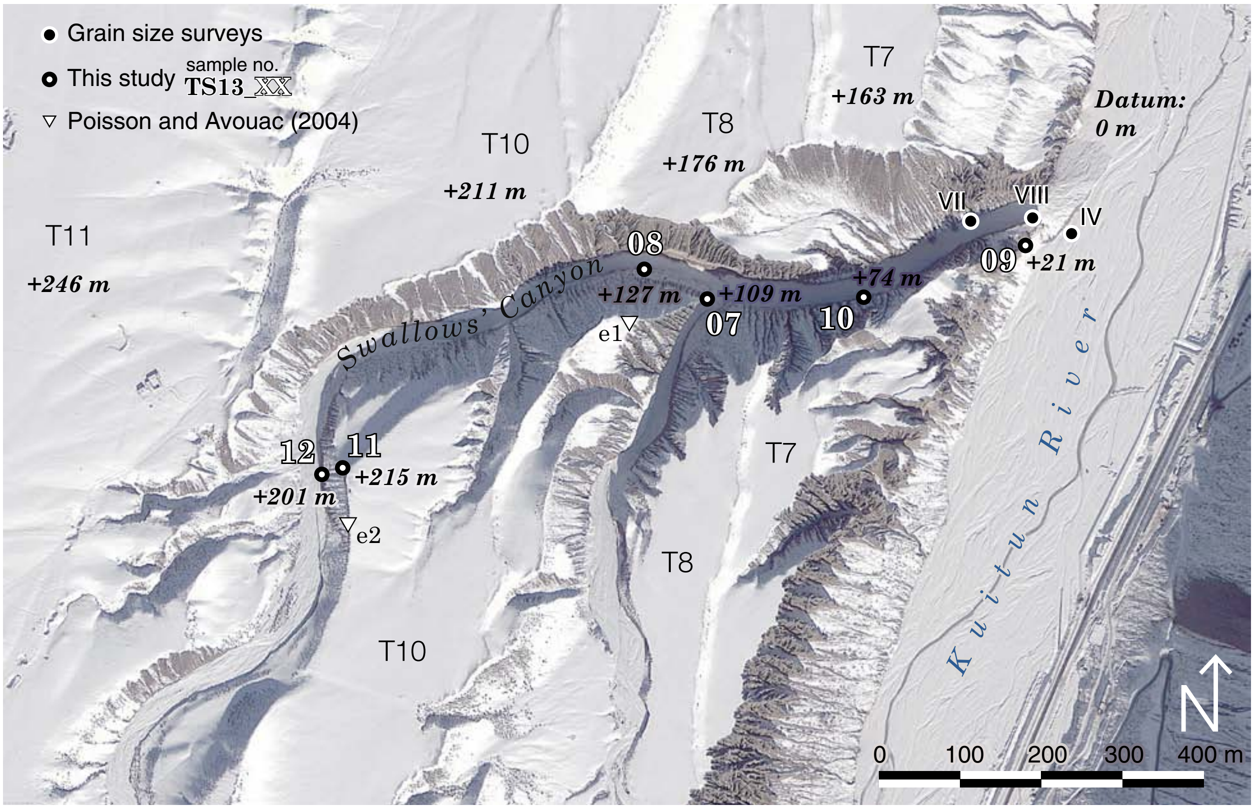

Fig. 7. Map of Swallows' Canyon with location of samples and grain size surveys. DigitalGlobe image (23.12.2012) accessed from Google Earth.

2004), and opening up a new dimension of the record with depositional ages of strata exposed in the canyon. Three samples were collected from the flight of terraces in the core of the Dushanzi anticline (Figs 2 and 5). Two other samples constrain abandonment of the terraces upstream of the anticline: on T10 at the top of Swallows' Canyon, in which the stratigraphic section was surveyed, and on T8 close to the apex (Figs 4 and 7). A summary of the samples collected along the Kuitun River is presented in Fig. 9.

The samples of the strath terraces of the Dushanzi anticlines were sampled on T7, T2, and T1, which respectively lie 123 m, 52 m and 3 m above the thalweg (Fig. 5). The abandonment age of T7 is determined at 7.7 ± 1.0 ka by the sample TS13_45 taken in the middle of a 0.3-m thick silt horizon capping the 1.5-m thick cobble conglomerate that lies on the strath of T7. The silt horizon is buried by a layer of colluvium. On T2, we sampled 20 cm above the contact between the *ca*. 4-m thick alluvial cobble deposit covering the strath and the 3.2 m fluvially reworked loess and fine sand layer that caps it. This sample gives a minimum abandonment age for T2 at 3.3 ± 0.3 ka that corresponds to the age of two charcoal samples from T2 radiocarbon-dated by Poisson & Avouac (2004) at 3.33 ± 0.04 ka and 3.4 ± 0.2 ka (C-T5-1 and C-T5-2). The final sample (TS13_37) was collected on T1 5 cm above the fluvial fill in 0.8 m of clayey fine sand to silt with few granules. The fluvial fill is 3.2-m thick and lies on the bedrock strath of T1 that is only 1.6 m above the low flow river. The minimum age of abandonment of the lowest terrace T1 is 1.7 ± 0.4 ka. This luminescence age corresponds to the maximum age constraint from a charcoal taken from the same reworked loess cap and dated at 1.71 ± 0.04 ka by Yang *et al.*, 2013). The new dates for the Kuitun River terraces, and in particular the confirmation of the relatively old age of the most recent very low terrace suggest that the river started incising around 13 ka and that incision rates increased to at least 30 mm year^{-1} at the anticline until 1.7 ka when the river almost entirely ceased to incise vertically (Fig. 10).

At the top of Swallows' Canyon, we collected TS13_11 in a silt lens at the base of the colluvium wedge that caps the alluvial tread of terrace T10. The resulting abandonment age is 13.4 ± 1.6 ka which is somewhat older than sample KTN-09 taken below the same colluvial cover 100 m farther south and dated at 10 ± 2 ka by Poisson & Avouac (2004). TS13_86 is sampled on T8 in a silt horizon 20 cm above the fluvial deposit of the terrace and below a wedge of colluvium. It yields an age of 9.1 ± 1.3 ka. Terrace T8 is found on either sides of the river and can be followed to the anticline (Fig. 4).

Table 1. Results of post-IR IRSL luminescence (pIRIR) and cosmogenic (TCN) dating of terraces and stratigraphy with location details. The river acronyms are KTN (Kuitun), AJH (Anjihai), TDO (Toudao), and MNS (Manas). Targets are either terraces (T#) or stratigraphy (S). The relative height* is the elevation of the sample above the river divided by the height of the fill terrace marking the onset of incision. If an incision episode is only documented by a single terrace, it is assumed to be a fill terrace with elevation 1

Field code	River	Target and method	Height*	Latitude (°N)	Longitude (°E)	Elevation (m.a.s.l.)	Age (ka)
TS13_37	KTN	T1 (pIRIR)	0.02	44.2962	84.7885	734	1.7 ± 0.4
TS13_36	KTN	T2 (pIRIR)	0.32	44.2919	84.7873	809	3.3 ± 0.3
TS13_45	KTN	T7 (pIRIR)	0.76	44.2884	84.7819	865	7.7 ± 1.0
TS13_86	KTN	T8 (pIRIR)	0.65	44.1551	84.7533	1169	8.4 ± 0.7
TS13_11	KTN	T10 (pIRIR)	1.00	44.2123	84.7673	1118	13.4 ± 1.6
TS13_02	KTN	S (pIRIR)	0.05	44.1408	84.7354	976	286.1 ± 40.9
TS13_09	KTN	S (pIRIR)	0.09	44.2154	84.7805	924	316.9 ± 24.3
TS13_01	KTN	S (pIRIR)	0.10	44.3260	84.7794	705	116.8 ± 8.1
TS13_10	KTN	S (pIRIR)	0.30	44.2146	84.7772	977	396.5 ± 36.7
TS13_07	KTN	S (pIRIR)	0.44	44.2145	84.7739	1012	193.4 ± 28.0
TS13_08	KTN	S (pIRIR)	0.52	44.2149	84.7727	1030	48.9 ± 3.6
TS13_03	KTN	S (pIRIR)	0.67	44.3685	84.7927	680	18.3 ± 2.6
TS13_12	KTN	S (pIRIR)	0.82	44.2121	84.7668	1104	181.0 ± 13.0
TS13_14	AJH	T3 (pIRIR)	0.16	44.1008	85.0983	1189	1.7 ± 0.3
TS13_19	AJH	T13 (pIRIR)	0.88	44.0929	85.0986	1377	3.6 ± 0.3
TS12-ANJ-T1B	AJH	T18 (TCN)	1.00	44.1052	85.0973	1424	5.1 ± 1.7
TS13_35	TDO	T- (pIRIR)	1.00	43.9794	85.1070	1783	37.4 ± 6.4
TS13_32	TDO	T- (pIRIR)	1.00	43.9734	85.1261	2063	111.0 ± 7.0
TS13_34	TDO	T- (pIRIR)	1.00	43.9738	85.1255	2064	236.1 ± 26.3
TS13_30	MNS	T- (pIRIR)	0.95	43.8489	85.8011	1189	81.3 ± 9.0
TS13_33	MNS	T- (pIRIR)	0.80	43.8489	85.8014	1158	198.1 ± 20.5

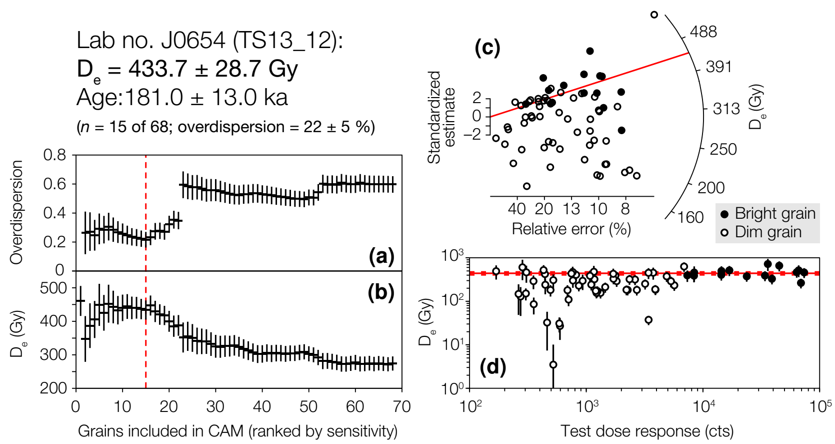

Fig. 8. The relationship between grain brightness (i.e. sensitivity) and equivalent dose is shown for sample J0654. (a) By incrementally increasing the number of grains included in the Central Age Model, the overdispersion reaches a minimum when the brightest 15 grains are included. (b) The effect of adding the next-dimmest grain to the calculation of D_e is illustrated. (c) A radial plot of all single-grain De values shows the wide range in apparent burial doses. By selecting only the brightest 15, however (shown as filled circles), a finite depositional age is apparent, with an overdispersion within the expected range (20% ± 9% Arnold & Roberts, 2009) for a well-bleached population: 22%. (d) The D_e values of individual grains are plotted against their response to a test dose of 35 Gy. The mean and standard deviation (1σ) of the population is shown as a solid and two dashed lines, respectively.

Five samples documenting the aggradation time frame of the canyon walls were taken in the steep tributary Swallows' Canyon. A 246-m section of rounded pebble to cobble conglomerate, either matrix or clast-supported, is exposed in the canyon (Fig. 7). It holds rare silt to sand cross-bedded lenses of thickness 5–30 cm suitable for luminescence dating. In Swallows' Canyon, the five samples TS13_09, TS13_10, TS13_07, TS13_08 and TS13_12 are found at elevations of 21, 74, 109, 127 and 201 m above the thalweg and increasing distance from the

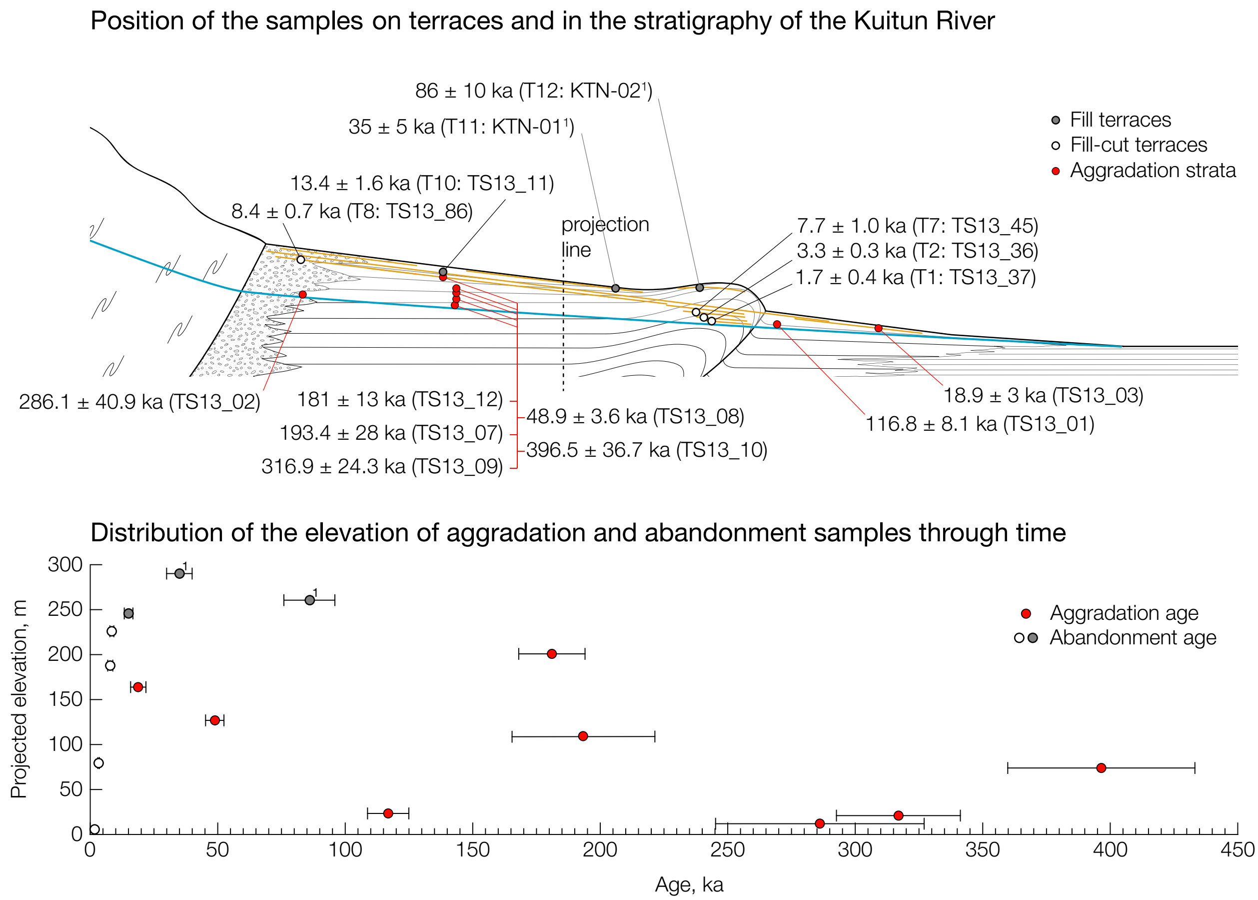

Fig. 9. Samples collected along the Kuitun River. Top: position of all the samples in a sketch of the river system. Bottom: elevation of the samples above the river. To compare the samples with each other, all samples are projected on a central vertical transect where T10, the most recent fill terrace, lies 245 m above the river and by multiplying that height by the fraction of the local height of T10 they lie at. All data from this study except for 1) Poisson (2002).

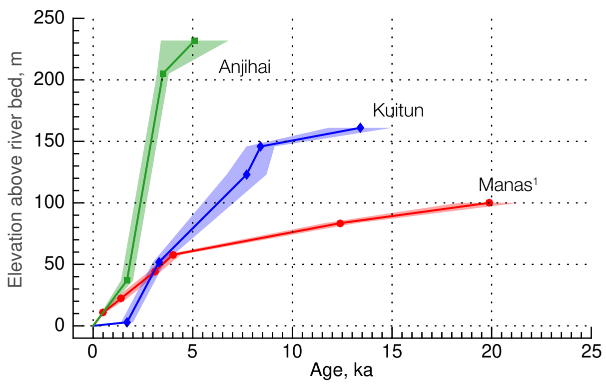

Fig. 10. Abandonment age and elevation above the river of the terraces documenting the entire most recent incision episode in the Kuitun, Anjihai, and Manas Rivers. The samples in each river are from the same reach and no correction is applied to their height. (1) Manas data from Gong *et al.* (2015), all other samples from the present study.

river's left edge of the floodplain of 30, 230, 480, 590 and 930 m respectively (Fig. S9 in Appendix S1). TS13_09 is sampled in a 15-cm thick lens of silt to medium sand. TS13_10 is taken from a 10- to 15-cm thick lens of silt to fine sand. TS13_07 is sampled in a 20-cm thick lens of silt to fine sand. TS13_08 is sampled in a 5-cm thin lens of silt that held few grains of the target size (175–200 μm) and only 4/5 grains were used. Finally TS13_12 is sampled in a 10- to 15-cm thick lens of silt to medium sand. The ages we obtained from bottom to top are respectively 316.9 ± 24.3 ka, 396.5 ± 36.7 ka, 193.4 ± 28.0 ka, 48.9 ± 3.6 ka and 181.0 ± 13.0 ka.

At the fan apex, the aggradation sample TS13_02 was taken in the river's right wall, 15 m above the thalweg where the total depth of the canyon is 308 m. It was collected in a 1.5-m thick fluvial silt to fine sand horizon wedged between pebble to boulder conglomerates. The age of this layer is 286.1 ± 40.9 ka. The first of the two downstream samples, TS13_01, was taken in a 0.5 m short lens of fluvial silt to fine sand and gives an age of 116.8 ± 8.1 ka. The lens lay 10 m above the thalweg, in the river's left wall, where the canyon is 105 m deep, 420 m north of the frontal thrust. The last sample, TS13_03, was taken in a terrace riser on the river's right 40 m above the river for a total incision of 60 m. The target was a thin lens of silt which yielded an age of 18.9 ± 3.0 ka.

Results for the Anjihai River

Along the Anjihai River, we focused the dating effort on a flight of 18 Holocene terraces (Fig. 6). The terraces (T1–T18) are preserved at the junction of the Anjihai and Toudao Rivers. The flow of both streams directs erosion away from the terrace flight, preserving the flight in its wake. The total incision at the location of the terrace flight is 238 m. The pace of incision is documented by the TCN profile TS12_ANJ-T1B on the highest terrace T18 and by two post-IR IRSL ages sampled on the terrace flight: TS13_19 on T13 and TS13_14 on T1. Luminescence targets are scarce on these terraces due to very thin loess cover and important bioturbation of the treads. The abandonment age of T18 is 5.1 ± 1.7 ka (TS12_ANJ-T1B) and corresponds to the timing of abandonment of the same surface at the windgap between the Halaande and Anjihai Anticlines to the north (Fig. 3) dated at 5.3 ± 0.3–4.1 ± 0.2 ka to 3.7 ± 0.2–3.5 ± 0.2 ka by Fu *et al.* (2017) with OSL and post-IR IRSL dating (AJH-03, AJH-05, AJH-04, AJH-02). The two post-IR IRSL samples we obtained for T13 and T1 yield ages of 3.6 ± 0.3 ka and 1.7 ± 0.3 ka respectively. These ages imply a local incision rate peaking at 93^{+47}_{-23} mm year^{-1} between *ca.* 3.6 and 1.7 ka. Since the abandonment of the youngest terrace 37 m above the riverbed, the incision rate decreased to 22 ± 4 mm year^{-1} (Fig. 10).

Upstream from the terrace flight, the Toudao River is incised through Jurassic foreland deposits after leaving the mountain range. The Jurassic series can be easily identified in satellite images using coal mines as markers. The incised floodplain is flanked by a terrace that projects into the highest terrace of the flight downstream. The terrace is, however, partly covered by colluvium derived from the valley flanks. We collected a sample (TS13_35) in a silt horizon 5–10 cm above the cobble conglomerate that fills the valley and at the base of ~10 m of fine-grained colluvium. The sampled layer had only few grains of the target size (175–200 μm) and only 6/7 grains were used. The sample constrains the minimum age of abandonment of fluvial aggradation at 37.4 ± 6.4 ka. This corresponds to a similar age of abandonment as the Kuitun terrace T11 at 35 ± 5 ka (Fig. 4; Poisson, 2002).

We collected two samples overlooking the Toudao River at the edge of a gently sloping pasture draining into the neighbouring Jingou River (Fig. 3). The Toudao River flows more than 250 m below the edge of the pasture. The road outcrop of these samples exposes 10–20 m of coarse sand to cobble-sized fluvial deposits with few thin lenses of silt to medium sand (Fig. S19 in Appendix S1). The fluvial deposits cover a strath cut into Jurassic foreland deposits. The lowest of the two samples (TS13_34) is taken in a 10-cm thick silt lens, at the base of a 3- to 4-m thick massive fluvial conglomerate and 2.5 m above the bedrock strath. It yields an age of 236.1 ± 26.3 ka. The second sample (TS13_32) is taken in the first silt lens above the massive fluvial cobble conglomerate and below a few thinner pebble conglomerate horizons. It lies 3–4 m higher in the stratigraphy, about 60 m farther to the southeast and has an age of 111.0 ± 7.0 ka.

Results for the Manas River

The samples from the Manas River are taken from a wide strath terrace cut into north dipping Jurassic and Cretaceous foreland deposits directly at the outlet of the high range (Figs 2 and 3). The surface of the strath exposed along the canyon has multiple levels indicating different episodes of cutting (Fig. 2). The samples, TS13_33 and TS13_30, constrain the deposition and abandonment of a section of the alluvium on the wide strath terrace. The alluvium cover is made of a *ca.* 10-m thick clast-supported conglomerate ranging from boulder to pebble from base to top. The conglomerate is covered by a discontinuous layer of silt to fine sand with a maximum thickness of 20 cm. The fine-grained layer is capped by *ca.* 1.5 m of angular to subangular cobble to pebble colluvium and soil. TS13_33 was collected 2.5 m above the strath in a pocket of silt wedged between boulders. The aggradation age of the base of that cobble conglomerate is 198.1 ± 20.5 ka and the age of the cap above the conglomerate is 81.3 ± 9.0 ka (Fig. S22 in Appendix S1).

MORPHOLOGICAL EVOLUTION OF THE PIEDMONT

The anticlines of the fold-and-thrust belt in the northern piedmont are truncated in several places (Fig. 3). Most of these gaps are canyons occupied by the active rivers that are incised in the anticlines and in the alluvial fans upstream and downstream. Others are windgaps that lie flush with abandoned fan surfaces only offset by several metres high fault scarps at the deformation front (Avouac *et al.*, 1993; Gong *et al.*, 2015). These windgaps were cut by the rivers that followed different courses in the past. In order to maintain the gaps, the rivers must have occupied them frequently. The rivers presumably migrate when the fans are fully aggraded. The presence of multiple gaps across the anticlines thus testifies of repeated episodes of aggradation and incision.

Kuitun River

We can establish a detailed record of the Holocene incision in the Kuitun River thanks to the nine Holocene terraces preserved in the Dushanzi Anticline. The new ages complete the incision history of the Kuitun River and reveal that the river largely ceased to incise at 1.7 ± 0.4 ka (TS13_37, Fig. 10). The fluvial incision rate at the anticline since 1.7 ± 0.4 ka cannot be precisely calculated because the exact elevation of the bedrock strath in the middle of the channel is unknown. The abandoned strath lay 1.6 m above the water edge in June 2013 and the water was at least 1 m deep from visual inspection giving an incision rate of at least 1.5 mm year^{-1} since 1.7 ± 0.4 ka. This rate of incision corresponds well to a newly estimated Holocene uplift rate of the anticline of $1.49^{+0.20}_{-0.16}$ mm year^{-1} calculated from the 20 m of vertical offset recorded by the deformation of T10 (Poisson & Avouac, 2004) and our single-grain post-IR IRSL age for T10 of 13.4 ± 1.6 ka (TS13_11). We favour this new data point over the 10 ± 2 ka multi-grain OSL age of Poisson & Avouac (2004) because of the high dispersion observed with single-grain measurements (see Fig. S7 in Appendix S1) that goes unnoticed in a multi-grain measurement. Upstream from the anticline, the river flows on a straight path and there, the youngest preserved terrace is T7 (TS13_45 at 7.7 ± 1 ka). Without the age constraint of the lowest terrace in the anticline (1.7 ± 0.4 ka at 5 m above the channel, sample TS13_37), the tall walls of the canyon give the impression that the river is still incising at a very high rate. However, when vertical incision stalls, like in the Kuitun valley since 1.7 ± 0.4 ka, ongoing lateral erosion erodes the valley walls and systematically destroys the youngest terraces, carving a rectangular cross-section (Malatesta *et al.*, 2017). The rectangular valley cross-section implies a period of stalled vertical river incision, rather than fast ongoing incision that started with the abandonment of T8 and T7 as previously thought (Poisson & Avouac, 2004).

The new deposition ages in the stratigraphy of the Kuitun fan combined with the terrace abandonment ages allow the study of the river aggradation and incision history. The combination of abandonment and aggradation ages of this fluvial system indicates repeated episodes of aggradation and incision over the last 450 kyrs. While the fill terraces constrain the maximum elevation reached by the river, the aggradation samples only provide a minimum depth for past river incision. To compare the relative elevations of these samples taken at various positions along the stream, where the canyon depths range from 60 to 308 m (Fig. 9, top), we project each elevation above the river to a central section where T10 is 246 m above the river (Fig. 9, bottom) and assume that the river incises and aggrades around a pivot at the fan toe with a uniform gradient. The elevation of the 86 ± 10 ka terrace T12 is restored to its initial position by removing the accumulated uplift (at Holocene rate $1.49^{+0.20}_{-0.16}$ mm year^{-1}) that raised it 150 m above T10 since abandonment. Between the terrace T10 that marks the onset of the youngest incision and the next older terrace (T11 at 35 ± 10 ka, KTN-01), we document a phase of aggradation one-third down the existing canyon at 18.9 ± 3 ka (TS13_03). Similarly, terraces T11 and T12 (called F_K and Q_3 by Poisson & Avouac, 2004) are separated by a phase of aggradation documented at 48.9 ± 3.6 ka (TS13_08). Three successive incisional episodes separated by aggradation phases can be thus identified in the last 100 kyrs. No well-defined terraces older than T12 have been found that could place the maximum elevation of the river at earlier stages.

Nine-tenths down the existing canyon, we can further document an aggradation phase at 112.4 ± 45.8 ka (TS13_01) that would have been shortly followed by terrace T12 on top of the canyon. Before that, two additional ages in Swallows' Canyon bracket a period of aggradation between 193.4 ± 28 ka and 181.0 ± 13.0 ka (samples TS13_07 and TS13_12) at a depth of three- to one-fifth (s) of the modern canyon depth (102–10 m below the Holocene fill terrace). A phase of incision had to follow it to bring the river down to the level of TS13_01. The two samples around 180 ka (TS13_07 and TS13_12) lie stratigraphically below and above TS13_08 at 48.9 ± 3.6 ka. As these are 110 and 340 m away from the river, this age inversion is a likely sign of truncation of the strata by an incision phase between the two ages (Fig. S9 in Appendix S1). Three additional ages collected near the level of the modern Kuitun River (TS13_02, TS13_09 and TS13_10) indicate aggradation phases between 286.1 ± 40.9 and 396.5 ± 36.7 ka. These ages lie near the methodological limit of luminescence dating and the nonlinear fading correction results in very large uncertainties (see methods). We are not able to identify distinct phases of aggradation with these older samples, but they indicate that the sediment remobilised by Holocene incision contained material deposited between the latest aggradation phase *ca.* 15 and 20 ka and the Middle Pleistocene, a time span representing five glacial periods.

The grain sizes in the active channel of the Kuitun River largely reflect those supplied by the valley walls. The only significant trend in the channel grain size is a rapid loss of very coarse material near the apex (Fig. S2 in Appendix S1). The bedrock channel upstream from the apex is not gravel bedded and holds cobbles and boulders, but we were not able to access and survey it. We have not surveyed sediment grain size at the dated horizons, but we sampled the bed of the tributary canyon and a small fan collecting sediment at the foot of a chute in the canyon wall. These surveys integrate sources across the stratigraphic stack above the sampling site. The similarity between the walls and the stream bed as well as the drop in D_{84} away from the apex are clear signs that the bedload consists overwhelmingly of material currently eroded from the fan. Given how grain size on alluvial fans can coevolve with changing climate (D'Arcy *et al.*, 2017), it would be informative to survey the D_{50} at each dated horizon.

Anjihai River

The samples documenting aggradation of fluvial conglomerate on the bedrock strath, now located 250 m above the Toudao River (TS13_32 and TS13_34) suggest a former northeast path of the smaller river that must have bevelled the foreland deposits and flowed towards the Jingou River over what is now a gently sloping pasture (highlighted by an arrow in Fig. 3). The bevelling of the foreland must have occurred prior to 236.1 ± 26.3 ka and the river abandoned that course to flow northwards after 111.0 ± 7.0 ka. The modern northward course is the steepest descent for this river and the change of path could be the result of a capture from the main trunk of the Anjihai River after erosion through the Jurassic foreland deposits.

Manas River

The large strath of the Manas River, right after leaving the high range, has been cut in tilted Jurassic and Cretaceous series. The sample collected in conglomerate 2.5 m above the strath constrains the minimum age of strath creation at 198.1 ± 20.5 ka (TS13_33). The last time the river aggraded high enough to resurface the tread of the terrace is at 81.3 ± 9.0 ka (TS13_30).

PLEISTOCENE CLIMATE AND AGGRADATION–INCISION CYCLES

Pleistocene climate

The Junggar Basin and the piedmont are semi-arid and most precipitation at present is derived from the Westerlies and falls in early summer; the rest falls as snow in the high range during fall and winter (Cheng *et al.*, 2012; Sorg *et al.*, 2012). The hydrograph of the rivers is dominated by the melt season with peak discharges between June and August (Poisson, 2002; Liu *et al.*, 2011). Past climate dynamics in the region have been reconstructed from caves in the Tian Shan (Cheng *et al.*, 2012, 2016b; see Fig. 1 for location of the Kesang Cave), from sedimentary and pollen studies in Lake Manas (Fig. 1; Jelinowska *et al.*, 1995; Rhodes *et al.*, 1996; Fan *et al.*, 2012), from lake level reconstructions of Ebi Nor Lake (Fig. 1; Poisson, 2002) and of lakes in Northwest China (Liu *et al.*, 2011). The larger scale climate dynamics are captured by speleothem records, of the main moisture source in the Eastern Mediterranean (Bar-Matthews *et al.*, 1997), carried to Central Asia by the Westerlies, and of a potential second southern source from the East Asian Summer Monsoon (EASM; Wang *et al.*, 2001, 2008) and the Indian Summer Monsoons (ISM; Kathayat *et al.*, 2016).

It has been proposed that monsoonal moisture could reach the Tian Shan during interglacials if the ISM is strong enough to cross the Tibetan Plateau (Gasse *et al.*, 1991) and/or if the EASM extends deep inland from the east (Cheng *et al.*, 2012). Increased insolation during interglacials allows the EASM to reach deeper into Central Asia every 120 kyr, due to a northward shifted Intertropical Convergence Zone (ITCZ) and associated monsoonal circulation (Schneider *et al.*, 2014). Conversely, a southward-shifted ITCZ prevents significant incursion of the ISM and EASM into Central Asia during the entire glacial period (Schneider *et al.*, 2014). Meanwhile, the Westerlies bring moisture recycled from the Atlantic realm into Central Asia during both glacial and interglacial periods, and have been argued to be antiphased to the EASM during interglacial periods (Nagashima *et al.*, 2011). Consequently, the EASM is only strong enough to influence the Tian Shan during these interglacial insolation maxima, whereas for most of the time, the Westerlies are the main factor with regard to moisture supply. The northeast Tian Shan would, however, receive varying amounts of Westerlies moisture during the precessional cycles. Observations from the western European seaboard suggest that insolation changes drive the North Atlantic sea ice dynamics, which in turn affect the mean latitudinal position of the Westerlies (Brauer *et al.*, 2008; Bakke *et al.*, 2009). The driest conditions are expected when the Westerlies are at their northern limit during high insolation and weak Siberian High (thus bypassing the Tian Shan in the north), and when they are confined west and south of the Pamiro-Alai-Tian Shan mountains during low insolation and strong Siberian High (Schneider *et al.*, 2014; Wolff *et al.*, 2016; Cai *et al.*, 2017). The largest intrusion of moisture is expected as the Westerlies shift from one end-position to the other and sweep across Central Asia, as found in various archives (Vandenberghe *et al.*, 2006; Chen *et al.*, 2010; Nagashima *et al.*, 2011; An *et al.*, 2012).

The water and sediment fluxes that control sedimentary dynamics on the piedmont are affected by variations in temperature and precipitation. Cooler temperatures, together with higher precipitation, support extensive glaciation, and enhanced sediment production by glacial and periglacial processes (Molnar & England, 1990; Brozovic *et al.*, 1997; Zhang *et al.*, 2001; Herman *et al.*, 2013). In Central Asia, the low temperatures and dry conditions of the stadial periods would increase glacial and periglacial erosion in the high mountain while little water discharge is available to transport and evacuate glacial and periglacial sediments.

River incision and climate since 30 ka

With the new dates presented here and the terrace ages reported by Poisson (2002), Poisson & Avouac (2004), Lu *et al.* (2010a), Gong *et al.* (2014), Lu *et al.* (2014) and Stockmeyer *et al.* (2017), we can constrain recent fluvial incision by the Kuitun, Anjihai, Jingou and Manas Rivers in unprecedented detail. Entrenchment of the rivers Kuitun, Anjihai and Manas is each measured in a unique terrace flight (Fig. 3). The Jingou record, however, is a composite from different reaches along the river. To compare the relative incision of the four rivers with each other, we normalise the elevation above the river of all terraces by the local height of the fill terrace that marks the onset of incision (Fig. 11a). It was known that all rivers had incised rapidly during the Holocene, but insufficiently detailed sampling gave the impression of an apparent synchronous incision (Avouac *et al.*, 1993; Molnar *et al.*, 1994). Here we show that the onset of incision and its slowdown were not synchronous across the piedmont. The onset of incision varies by *ca.* 8 kyrs with the Kuitun River starting at 13 ka and the Anjihai River at 5 ka. The Kuitun River has stopped incising at 2 ka, with the incision rate measured in the anticline today matching that of its uplift. The Manas River, on the other hand, appears to not have reduced its incision rate yet, suggesting that the equilibrium profile is still far from reached. Collectively, the four rivers indicate individual transitions from aggradation to incision around the early Holocene and an acceleration of incision rates between 5 and 3 ka.

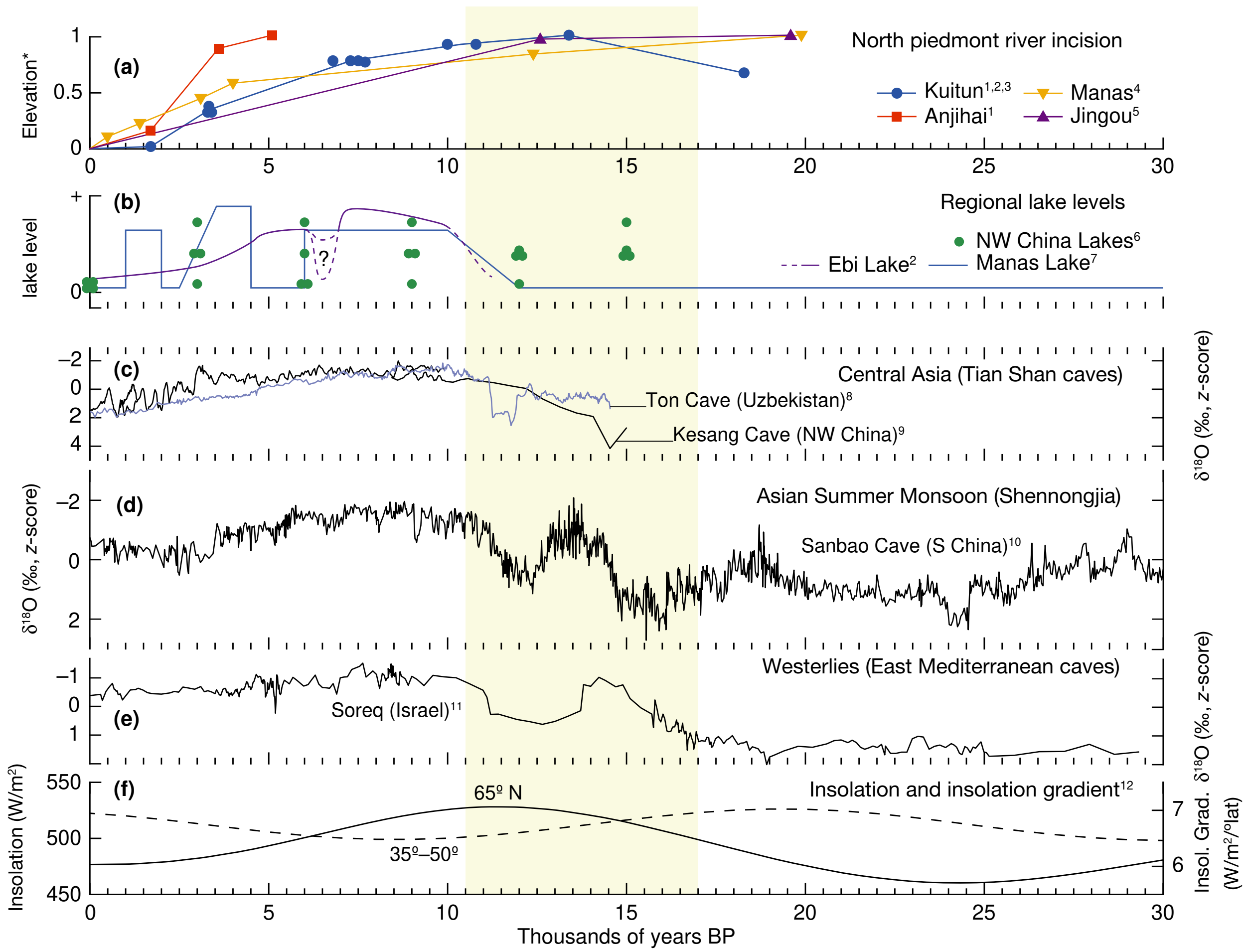

Fig. 11. Evolution of climate and incision four surveyed rivers of the north piedmont in the last 30 kyrs. Rivers incise as the region becomes warmer and more humid, yet the onset and pattern of incision is different for each of them, suggesting that it is not directly driven by the contemporary climate change. The yellow band highlights the last deglaciation. (a) Youngest incision phase in four rivers of the piedmont and the last documented aggradation for the Kuitun River; (1) this study; (2) Poisson (2002); (3) Poisson & Avouac (2004); (4) Gong *et al.* (2014); (5) Lu *et al.* (2010a). (b) Regional lake levels; (6) Yu *et al.* (2001); (7) Rhodes *et al.* (1996). (c) $\delta^{18}O$ values for the Central Asian record of the Kesang and Ton Caves; see Fig. 1 for location of Kesang; (8) Cheng *et al.* (2012); (9) Cheng *et al.* (2016b). (d) $\delta^{18}O$ for the Asian Summer Monsoon; (10) Cheng *et al.* (2016a). (e) $\delta^{18}O$ values for the Westerlies; (11) Bar-Matthews *et al.* (1997). (f) insolation at 65°N and insolation gradients between 35°N and 50°N; (12) Berger (1978).

A climate record from diverse regional archives allows us to compare the fluvial dynamics discussed above with effective moisture budget around the Junggar Basin since the LGM (Fig. 1). Sedimentological and palynological data from a sediment core of Lake Manas indicate a period of increased effective moisture starting at 10 ka after a very arid period and finishing at 1 ka with two dry episodes at 5 and 3 ka (Fig. 11b; Rhodes *et al.*, 1996). The lake level reconstruction for Ebi Nor provided by Poisson (2002) shows a similar trend with the lake reaching a high stand at the onset of the Holocene and decreasing to the current low level after 5 ka (Fig. 11b). Additionally, data from four NW China lakes by Yu *et al.* (2001) provide a larger scale proxy for Central Asian moisture with a period of increased moisture around 15–5 ka, followed by increased aridity leading to today's dry conditions (Fig. 11b). The high stand of the lakes reflects increased moisture during the Mid-Holocene Thermal Optimum with a lag of a few kyr. That is due to high evaporation rates preventing high lake levels at the peak of the Thermal Optimum (Rhodes *et al.*, 1996; Cheng *et al.*, 2016b; Cai *et al.*, 2017). The association of warm and wet conditions stands in contrast to the dry and cold climate characterising the glacial maxima in Central Asia (Cheng *et al.*, 2012). Finally, in the modern dry and warm conditions, glaciers are mostly confined to cirques (Stroeven *et al.*, 2013). The post-LGM increase in temperature is also recorded by the speleothem δ^{18}O record from Kesang Cave (Figs 1 and 11f; Cheng *et al.*, 2012; Cai *et al.*, 2017).

Incised fans downstream of semi-glaciated catchments reflect climatic forcing but the precise onset and pattern of incision recorded by terraces cannot be used to directly date the forcing. It depends on the local timescale of sediment evacuation from the high range and varies between the catchments. Furthermore, the vertical incision response of a river to a drop in input Q_s/Q_w depends on the partition between horizontal and vertical erosion and on autogenic feedbacks with the valley walls that promote accelerated vertical incision during entrenchment (Malatesta *et al.*, 2017).

Our interpretation of the evolution of the rivers in the context of climatic forcing since 30 ka is represented in Fig. 11c–f. The phase of sediment evacuation and fan aggradation corresponds to the period of deglaciation, when the extensive glaciers of the LGM started to retreat under increasingly warm and wet conditions, exposing moraine and hillslope deposits to greater water discharge that could evacuate them out of the mountain range and onto the piedmont. We use a simplified and idealised scenario for the Eastern Tian Shan deglaciation. An ice core in the Kyrgyz Tian Shan shows a more complicated post-LGM history with glacial advance at the Younger Dryas (Takeuchi *et al.*, 2014). A detailed history of deglaciation in each studied catchment could inform the precise timing of sediment evacuation. The last deglaciation is highlighted with the shaded yellow rectangle in Fig. 11. The changes in insolation of the precessional cycles are reflected in the δ^{18}O trends in proxies of regional moisture sources: the Westerlies, the Asian Summer Monsoon, and finally the local records of the Kesang and the Ton Caves (Fig. 11c–e). At the apex of the piedmont fans, the ratio Q_s/Q_w drops after the bulk of the sediment readily available in the high range is evacuated. This lower Q_s/Q_w value then causes incision of the oversteepened alluvial slopes. The onset of incision varies from one catchment to the other, depending on the size of the respective reservoirs of loose sediments upstream and the efficiency of reservoir evacuation.

Aggradation and incision since 150 ka

We can precisely constrain fluvial incision since the LGM, thanks to numerous fill-cut terraces. The task is more arduous for previous incision phases. The fill-cut terraces of older cycles have been buried and only an incomplete fill terrace record remains. The number of aggradation samples is too small to establish a precise stratigraphic model. We can nevertheless inform the sparse data with our understanding of aggradation–incision and climate in the last 30 kyrs to propose a history of aggradation and incision since 150 ka (Fig. 12, left part). The uncertainty on further age constraints between 150 ka and 450 ka is too large to establish the chronology of older aggradation–incision cycles (Fig. 12, right part). However, the ages > 150 ka imply that Late and Middle Pleistocene deposits are being eroded and injected in the modern sediment flux. We use yellow shading in Fig. 12 to mark stadial–interstadial transitions, when Central Asian climate transitions from cold and dry, to warmer and wetter as the Westerlies sweep across the continent. Following our interpretation of the last 30 kyrs (Fig. 11), we expect piedmont aggradation when glacial and periglacial sediments are evacuated during deglaciation and rising insolation; and incision to follow once the upstream sediment reservoir is emptied and the ratio Q_s/Q_w drops. We do not expect all fill terraces to be preserved because any aggradation episode higher than the previous one will bury its terrace tread. However, the presence of active anticlines that uplift and safeguard straths allows the identification of several contemporary incision episodes across the rivers that support the relationship proposed for the youngest incision phase. The entire data set is shown in Fig. 12a, with normalised elevation as in Fig. 11a. The compilation of ages with all the references and coordinates can be found in Table S4 of Appendix S1.

Most notably, terraces on the Kuitun, Jingou, Manas and Hutubi Rivers mark an onset of incision coinciding with the 85 ka insolation peak (Marine Isotope Stage 5a).

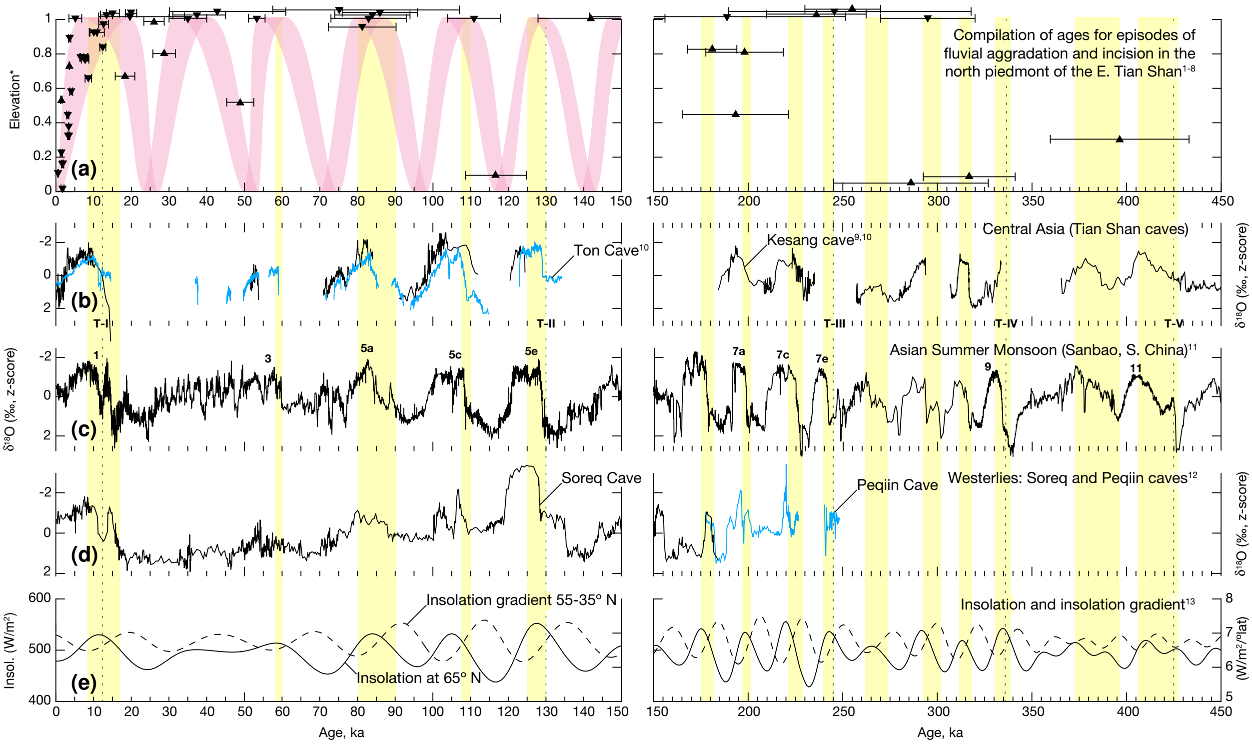

Fig. 12. Ages of the alluvial system with climate data since 450 ka. Clusters of abandoned terraces separated by aggradation episodes suggest fast and repeated cycles of aggradation and incision over the last 150 kyrs (suggested by the magenta tracks) and probably since 450 ka at least. Yellow bands highlight stadial–interstadial transitions. (a) terrace abandonment ages and stratigraphy aggradation ages in rivers of the Tian Shan north piedmont (detailed age compilation in Table S3 in Appendix S1); (1) this study; (2) Poisson (2002); (3) Poisson & Avouac (2004); (4) Lu *et al.* (2010a), (5) Lu *et al.* (2014); (6) Gong *et al.* (2015); (7) Fu *et al.* (2017); (8) Stockmeyer *et al.* (2017). (b) Climate sources: 1: δ^{18}O values for the Central Asian record of the Kesang and Ton Caves; (9) Cheng *et al.* (2012); (10) Cheng *et al.* (2016b). (c) δ^{18}O for the Asian Summer Monsoon; (11) Cheng *et al.* (2016a). (d) δ^{18}O values for the Westerlies; (12) Bar-Matthews *et al.* (1997). (e) insolation at 6N and insolation gradients between 35°N and 50°N; (13) Berger (1978).

Along the Manas River this interval marks the last time that the tread at the outlet of the high range was flooded and reworked, suggesting a particularly high episode of aggradation (TS13_33, Figs 2 and 3). Multiple terraces of the Kuitun, Anjihai and Jingou Rivers match the weaker insolation peak at 35 ka. Older ages have errors that span several insolation cycles and cannot be reliably attributed to one or the other. We note, however, a cluster of terrace ages around 240 ka at the penultimate interglacial (MIS 7e).

Based on the spacing of uplifted terraces on the active anticlines of the fold-and-thrust belt, Molnar *et al.* (1994) proposed that major phases of incision in the piedmont occurred at a 100 kyr frequency. But, instead of slow and continuous fan aggradation between the interglacial episodes of incision suggested by Molnar *et al.* (1994) and Poisson & Avouac (2004), we find repeated episodes of aggradation and incision, possibly in phase with the 21 kyr precession during the glacial period. These cycles are not driven by the summer monsoon which can only reach Central Asia under the atmospheric configuration of the interglacial period. The alluvial piedmont appears thus to repeatedly undergo large magnitude aggradation–incision cycles during the glacial periods which are governed only by the Westerlies. The glaciated upper catchments, acting as capacitors for sediment bedload, likely magnify the relatively small climatic changes in this hyper-continental region. Possibly, incision is deepest during interglacials if sufficient monsoonal moisture reaches eastern Central Asia (see the Section Pleistocene Climate), as for example during MIS 11 when higher effective moisture availability allowed speleothem growth in today's arid Gobi desert (Vaks *et al.*, 2013).

Stratigraphic perspective

The system contains two sediment capacitors: the high-range capacitor is made of the glacial valleys that collect glacial and periglacial sediments, and the piedmont capacitor driven by the alluvial aggradation–incision cycles that we describe and quantify in this study. The cycles of aggradation and incision in the piedmont delay the progradation of the coarse sediment load. They also change the composition of that flux as fluvial incision injects fluvial deposits as old as the Middle Pleistocene in the modern sediment flux. We describe here how this affects the downstream stratigraphy of the basin in a simple configuration. Figure 13a shows the progression of the sediment flux in the basin as a Wheeler-type diagram tracking the fine and the coarse load of a unique pulse. Final sediment deposition is marked by the shaded area. The transient presence of bypass material en route to the basin is indicated with a thinner outline and no shading. The coarse bedload material progresses more slowly than the suspended and dissolved loads that essentially move together with the water. The coarse material is first deposited on the upper fan before being remobilised by the subsequent incision. Downstream of the zone of initial aggradation, the sediment flux contains recycled older sediments. The difference in progression rate of the two loads leads to a hiatus between the two where they overlap. By swapping time for stratigraphic height, we build the basin and the foreland stratigraphy in Fig. 13b, assuming repetition of the same cycle. At the transition zone, the fine load that very quickly prograded into the basin is interfingered with the gravel front. Here, the sediments from the same initial pulse, a stadial–interstadial transition in the case of the north Tian Shan, are separated by a hiatus equal to the time necessary for the gravel front to cross the piedmont (Fig. 13c). In the northern piedmont, the hiatus is 6–15 kyrs long depending on the onset of incision. In the immensely larger Indus drainage, Clift & Giosan (2014) estimated a similar lag of 7–14 kyrs. If both systems are characterised by a similar lag, despite the difference in length scale, the buffering of the coarse load should be primarily dependent on the periodicity of forcing. Moreover, in the Kuitun River, the sediment composition downstream of the initial aggradation zone includes significant quantities of older recycled material ranging from the Middle Pleistocene to present.

Incision episodes in alluvial piedmonts can quickly mobilise a significant volume of sediment and impact the downstream stratigraphy, such that while the mountain range itself can act as a low pass filter damping environmental signals created by high-frequency climatic forcing (Castelltort & Van Den Driessche, 2003; Armitage *et al.*, 2013), alluvial piedmonts can amplify and record these signals by rapid reaction as documented here. High-frequency environmental signals sourced in alluvial piedmonts can be transferred along the alluvial domain (Simpson & Castelltort, 2012). However, they have a potentially limited downstream impact because they are

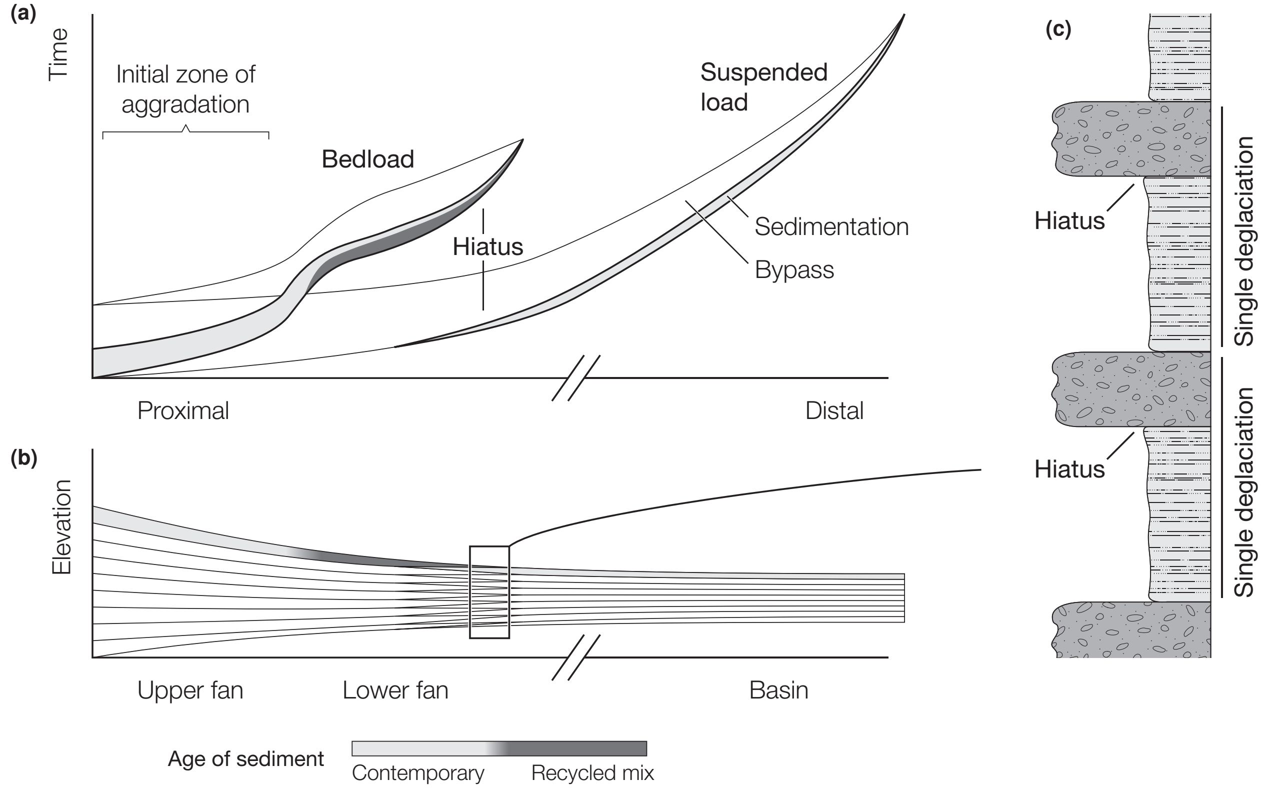

Fig. 13. (a) Propagation of the bedload and suspended load of a sediment pulse in a time vs. distance space (Wheeler-type diagram). The suspended load is immediately delivered to the basin. The bedload moves slowly, in two phases, first deposited directly in front of the high range and then remobilised by incision and transported to the foot of the piedmont (current situation in the north piedmont). The darker shade indicates bedload deposit with recycled material. (b) Collapse of the time vs. distance in spatial dimensions, assuming a repeated identical pulses. (c) The two deposits overlap at the transition basin-piedmont, and a hiatus of 6–15 kyrs separates the coarse and the fine sediment deposits initially produced by the same forcing.

carried by coarse grained sediments and are likely to only influence the gravel front, having little relevance for the stratigraphy farther downstream (Paola *et al.*, 1992; Armitage *et al.*, 2016). Furthermore, a reserve of coarse sediments that can be mobilised when water discharge increases will tend to stabilise the position of the gravel front by balancing the Q_s/Q_w ratio as suggested by Armitage *et al.* (2016).

CONCLUSIONS

This study extends the chronological constraints on the morpho-sedimentary evolution of the north piedmont of the Eastern Tian Shan with new ages of terrace abandonment and of strata exposed in the canyon walls of the entrenched Kuitun River.

We have shown that variations in temperature and moisture delivered by the Westerlies are the most likely cause of repeated aggradation and incision of the north piedmont. Glacial and periglacial erosion and fluvial sediment transport in the high range modulate the ratio of sediment flux and water discharge to the piedmont. The piedmont aggrades during stadial–interstadial transitions when sediments are evacuated under increasing insolation and resulting greater precipitation. Subsequent fast incision occurs after the upstream sediment reservoir is depleted and its timing does not directly depend on a direct external forcing. The nature of the control on the chronology of piedmont incision would need to be elucidated with a study of the upstream reservoir. Glaciated upper catchments act as high-range sediment capacitors that exacerbate the morphological reaction of the piedmont, which acts itself as another capacitor. The outward flux is affected by the capacitor effect of both systems.

Cycles of aggradation and incision in the north piedmont of the Eastern Tian Shan delay the flux of coarse material en route to the Junggar Basin by 6–15 kyrs. The temporary deposition of the coarse sediment load in the piedmont capacitor separates it from the finer load that is directly delivered to the basin. As a consequence, a depositional hiatus between the fine and coarse fractions of the same sediment pulse is expected where both facies overlap. In the Kuitun River, incision in the piedmont remobilises a mixture of sediments from the Middle Pleistocene to today and injects it in the modern sediment routing system.

ACKNOWLEDGEMENTS

The authors thank Sébastien Castelltort for his sedimentological insights. Stimulating discussions with Laure Guérit were most useful to design our work. Jess Adkins provided precious advice regarding the climatic considerations. We thank Stéphane Dominguez for his help collecting the sample TS12-ANJ-T1B. Two anonymous reviewers provided important inputs to improve the original manuscript. This study was supported by a PRF New Direction grant of the American Chemical Society (grant number: PRF #53814-ND8) and a Doc.Mobility fellowship of the Swiss National Foundation (project number: P1SKP2_158716) for L. C. Malatesta. This study received funding from the European Union's Horizon 2020 Research and Innovation program under the Marie Sklodowska-Curie grant agreement No 691037 to S.F.M. Breitenbach.

SUPPORTING INFORMATION

Additional Supporting Information may be found in the online version of this article:

Appendix S1. Details of sampling location, methods, and data set of compiled ages.

REFERENCES

Aitken, M.J. (1998) *An introduction to Optical Dating: The Dating of Quaternary Sediments by the Use of Photon-Stimulated Luminescence*. Oxford University Press, Oxford.

Allen, P.A. (1997) *Earth Surface Processes*. Wiley-Blackwell, Oxford.

Allen, P.A. (2008) Time scales of tectonic landscapes and their sediment routing systems. *Geol. Soc. Spec. Publ.*, **296**(1), 7–28.

Allen, P.A., Armitage, J.J., Carter, A., Duller, R.A., Michael, N.A., Sinclair, H.D., Whitchurch, A.L. & Whittaker, A.C. (2013) The Qs problem: sediment volumetric balance of proximal foreland basin systems – Allen – 2013 – Sedimentology – Wiley Online Library. *Sedimentology*, **60**, 102–130.

An, Z., Colman, S.M., Zhou, W., Li, X., Brown, E.T., Jull, A.J.T., Cai, Y., Huang, Y., Lu, X., Chang, H., Song, Y., Sun, Y., Xu, H., Liu, W., Jin, Z., Liu, X., Cheng, P., Liu, Y., Ai, L., Li, X., Liu, X., Yan, L., Shi, Z., Wang, X., Wu, F., Qiang, X., Dong, J., Lu, F. & Xu, X. (2012) Interplay between the Westerlies and Asian monsoon recorded in Lake Qinghai sediments since 32 ka. *Sci. Rep.*, **2**, 1–7.

Armitage, J.J., Dunkleyjones, T., Duller, R.A., Whittaker, A.C. & Allen, P.A. (2013) Temporal buffering of climate-driven sediment flux cycles by transient catchment response. *Earth Planet. Sci. Lett.*, **369**, 200–210.

Armitage, J.J., Burgess, P.A., Hampson, G.J. & Allen, P.A. (2016) Deciphering the origin of cyclical gravel front and shoreline progradation and retrogradation in the stratigraphic record. *Basin Res.*, 1–21. https://doi.org/10.1111/bre.12203.

Arnold, L.J. & Roberts, R.G. (2009) Stochastic modelling of multi-grain equivalent dose (De) distributions: implications for OSL dating of sediment mixtures. *Quat. Geochronol.*, **4**(3), 204–230.

AVOUAC, J.-P. & TAPPONNIER, P. (1993) Kinematic model of active deformation in Central-Asia. *Geophys. Res. Lett.*, **20** (10), 895–898.

AVOUAC, J.-P., TAPPONNIER, P., BAI, M., YOU, H. & WANG, G. (1993) Active thrusting and folding along the Northern Tien Shan and Late Cenozoic Rotation of the Tarim Relative to Dzungaria and Kazakhstan. *J. Geophys. Res.*, **98**(B4), 6755–6804.

BAKKE, J., LIE, Ø., HEEGAARD, E., DOKKEN, T., HAUG, G.H., BIRKS, H.H., DULSKI, P. & NILSEN, T. (2009) Rapid oceanic and atmospheric changes during the Younger Dryas cold period. *Nat. Geosci.*, **2**(3), 1–4.

BAR-MATTHEWS, M., AYALON, A. & KAUFMAN, A. (1997) Late quaternary paleoclimate in the Eastern Mediterranean Region from stable isotope analysis of Speleothems at Soreq Cave, Israel. *Quatern. Res.*, **47**(2), 155–168.

BERGER, A.L. (1978) Long-term variations of caloric insolation resulting from the earth's orbital elements. *Quatern. Res.*, **9** (2), 139–167.

BRAUCHER, R., DEL CASTILLO, P., SIAME, L., HIDY, A.J. & BOURLÈS, D.L. (2009) Determination of both exposure time and denudation rate from an in situ-produced 10Be depth profile: a mathematical proof of uniqueness. Model sensitivity and applications to natural cases. *Quat. Geochronol.*, **4**(1), 56–67.

BRAUCHER, R., MERCHEL, S., BORGOMANO, J. & BOURLÈS, D.L. (2011) Production of cosmogenic radionuclides at great depth: a multielement approach. *Earth Planet. Sci. Lett.*, **309**(1–2), 1–9.

BRAUER, A., HAUG, G.H., DULSKI, P., SIGMAN, D.M. & NEGENDANK, J.F.W. (2008) An abrupt wind shift in western Europe at the onset of the Younger Dryas cold period. *Nat. Geosci.*, **1** (8), 520–523.

BROWN, N.D., RHODES, E.J., ANTINAO, J.L. & MCDONALD, E.V. (2015) Single-grain post-IR IRSL signals of K-feldspars from alluvial fan deposits in Baja California Sur, Mexico. *Quatern. Int.*, **362**, 132–138.

BROZOVIC, N., BURBANK, D.W. & MEIGS, A.J. (1997) Climatic limits on landscape development in the northwestern Himalaya. *Science*, **276**(5312), 571–574.

BULL, W.B. (1977) The alluvial-fan environment. *Prog. Phys. Geogr.*, **1**(2), 222–270.

BULL, W.B. (1991) *Geomorphic Responses to Climatic Change*. Oxford University Press, New York, NY.

BURCHFIEL, B.C., BROWN, E.T., DENG, Q.D., FENG, X.Y., LI, J., MOLNAR, P., SHI, J.B., WU, Z.M. & YOU, H.C. (1999) Crustal shortening on the margins of the Tien Shan, Xinjiang, China. *Int. Geol. Rev.*, **41**(8), 665–700.

BUYLAERT, J.-P., MURRAY, A.S., THOMSEN, K.J. & JAIN, M. (2009) Testing the potential of an elevated temperature IRSL signal from K-feldspar. *Radiat. Meas.*, **44**(5–6), 560–565.

CAI, Y., CHIANG, J.C.H., BREITENBACH, S.F.M., TAN, L., CHENG, H., EDWARDS, R.L. & AN, Z. (2017) Holocene moisture changes in western China, Central Asia, inferred from stalagmites. *Quatern. Sci. Rev.*, **158**, 15–28.

CASTELLTORT, S. & Van Den DRIESSCHE, J. (2003) How plausible are high-frequency sediment supply-driven cycles in the stratigraphic record? *Sed. Geol.*, **157**, 3–13.

CHARREAU, J., CHEN, Y., GILDER, S., DOMINGUEZ, S., AVOUAC, J.-P., SEN, S., SUN, D., LI, Y. & WANG, W.-M. (2005) Magnetostratigraphy and rock magnetism of the Neogene Kuitun He section (northwest China): implications for Late Cenozoic uplift of the Tianshan mountains. *Earth Planet. Sci. Lett.*, **230**(1–2), 177–192.

CHARREAU, J., CHEN, Y., GILDER, S., BARRIER, L., DOMINGUEZ, S., AUGIER, R., SEN, S., GRAVELEAU, F. & WANG, Q. (2009) Neogene uplift of the Tian Shan Mountains observed in the magnetic record of the Jingou River section (northwest China). *Tectonics*, **28**(TC2008), 1–22.

CHARREAU, J., BLARD, P.H., PUCHOL, N., AVOUAC, J.-P., LALLIER-VERGÈS, E., BOURLÈS, D., BRAUCHER, R., GALLAUD, A., FINKEL, R.C., JOLIVET, M., CHEN, Y. & ROY, P. (2011) Paleo-erosion rates in Central Asia since 9 Ma: a transient increase at the onset of Quaternary glaciations? *Earth Planet. Sci. Lett.*, **304**(1–2), 1–8.

CHEN, F.-H., CHEN, J.-H., HOLMES, J., BOOMER, I., AUSTIN, P., GATES, J.B., WANG, N.-L., BROOKS, S.J. & ZHANG, J.-W. (2010) Moisture changes over the last millennium in arid central Asia: a review, synthesis and comparison with monsoon region. *Quatern. Sci. Rev.*, **29**(7–8), 1055–1068.

CHENG, H., ZHANG, P.Z. & SPÖTL, C. (2012) The climatic cyclicity in semiarid-arid central Asia over the past 500,000 years. *Geophys. Res. Lett.*, **39**(1), 1–5.

CHENG, H., EDWARDS, R.L., SINHA, A., SPÖTL, C., YI, L., CHEN, S., KELLY, M., KATHAYAT, G., WANG, X., LI, X., KONG, X., WANG, Y., NING, Y. & ZHANG, H. (2016a) The Asian monsoon over the past 640,000 years and ice age terminations. *Nature*, **534**(7609), 640–646.

CHENG, H., SPÖTL, C., BREITENBACH, S.F.M., SINHA, A., WASSENBURG, J.A., JOCHUM, K.P., SCHOLZ, D., LI, X., YI, L., PENG, Y., LV, Y., ZHANG, P., VOTINTSEVA, A., LOGINOV, V., NING, Y., KATHAYAT, G. & EDWARDS, R.L. (2016b) Climate variations of Central Asia on orbital to millennial timescales. *Sci. Rep.*, **6**, 1–11.

CLIFT, P.D. & GIOSAN, L. (2014) Sediment fluxes and buffering in the post-glacial Indus Basin. *Basin Res.*, **26**(3), 369–386.

D'ARCY, M. & WHITTAKER, A.C. (2014) Geomorphic constraints on landscape sensitivity to climate in tectonically active areas. *Geomorphology*, **204**, 366–381.

D'ARCY, M., WHITTAKER, A.C. & RODA, D.C. (2017) Boluda. Measuring alluvial fan sensitivity to past climate changes using a self-similarity approach to grain size fining, Death Valley, California. *Sedimentology*, **64**(2), 388–424.

DENGFA, H., SUPPE, J., GENG, Y., SHUWEI, G., SHAOYING, H., XIN, S., XIAOBO, W. & CHAOJUN, Z. (2005) Guide book for the field trip in south and north Tianshan foreland basin, Xinjiang Uygur Autonomous Region, China. *International Conference on Theory and Application of Fault-Related Folding in Foreland Basins*. Research Institute of Petroleum Exploration and Development, PetroChina, Beiging.

DUMITRU, T.A., ZHOU, D., CHANG, E.Z., GRAHAM, S.A., HENDRIX, M.S., SOBEL, E.R. & CARROLL, A.R. (2001) Uplift, exhumation, and deformation in the Chinese Tian Shan. *Geol. Soc. Am.*, Memoir: Palaeozoic and Mesozoic tectonic evolution of central Asia: From continental assembly to intercontinental deformation. **194**, 71–99.

DUNAI, T.J. (2010) *Cosmogenic Nuclides: Principles, Concepts and Applications in the Earth Surface Sciences*. Cambridge University Press, Cambridge.

Fan, A., Li, S.-H. & Chen, Y.-G. (2012) Late pleistocene evolution of Lake Manas in western China with constraints of OSL ages of lacustrine sediments. *Quat. Geochronol.*, **10(C)**, 143–149.

Fu, B.H., Lin, A.M., Kano, K., Maruyama, T. & Guo, J.M. (2003) Quaternary folding of the eastern Tian Shan, northwest China. *Tectonophysics*, **369**(1–2), 79–101.

Fu, X., Li, S.-H., Li, B. & Fu, B. (2017) A fluvial terrace record of late Quaternary folding rate of the Anjihai anticline in the northern piedmont of Tian Shan, China. *Geomorphology*, **278**, 91–104.

Fuchs, M. & Lang, A. (2001) OSL dating of coarse-grain fluvial quartz using single-aliquot protocols on sediments from NE Peloponnese, Greece. *Quatern. Sci. Rev.*, **20**(5–9), 783–787.

Galbraith, R.F., Roberts, R.G., Laslett, G.M., Yoshida, H. & Olley, J.M. (1999) Optical dating of single and multiple grains of quartz from Jinmium rock shelter, northern Australia: Part I, experimental design and statistical models. *Archaeometry*, **41**(2), 339–364.

Gasse, F., Arnold, M., Fontes, J.C., Fort, M., Gibert, E., Huc, A., Bingyan, L., Yuanfang, L., Qing, L., Mélières, F., Campo, E.V., Fubao, W. & Qingsong, Z. (1991) A 13,000-year climate record from western Tibet. *Nature*, **353** (6346), 742–745.

Gilbert, G.K. & Murphy, E.C. (1914) The transportation of debris by running water. *U. S. Geological Survey Professional Paper*, **86**, 1–263.

Gong, Z., Li, S.-H. & Li, B. (2014) The evolution of a terrace sequence along the Manas River in the northern foreland basin of Tian Shan, China, as inferred from optical dating. *Geomorphology*, **213(C)**, 201–212.

Gong, Z., Li, S.-H. & Li, B. (2015) Late Quaternary faulting on the Manas and Hutubi reverse faults in the northern foreland basin of Tian Shan, China. *Earth Planet. Sci. Lett.*, **424(C)**, 212–225.

Gosse, J.C. & Phillips, F. (2001) Terrestrial in situ cosmogenic nuclides: theory and application. *Quatern. Sci. Rev.*, **20**(14), 1475–1560.

Guan, S., Stockmeyer, J.M., Shaw, J.H., Plesch, A. & Zhang, J. (2016) Structural inversion, imbricate wedging, and out-of-sequence thrusting in the southern Junggar fold-and-thrust belt, northern Tian Shan, China. *AAPG Bull.*, **100**(9), 1443–1468.

Guerit, L., Barrier, L., Jolivet, M., Fu, B. & Métivier, F. (2016) Denudation intensity and control in the Chinese Tian Shan: new constraints from mass balance on catchment-alluvial fan systems. *Earth Surf. Proc. Land.*, **41**(8), 1088–1106.

Guralnik, B., Matmon, A., Avni, Y., Porat, N. & Fink, D. (2011) Constraining the evolution of river terraces with integrated OSL and cosmogenic nuclide data. *Quat. Geochronol.*, **6**(1), 22–32.

Hendrix, M.S., Graham, S.A., Carroll, A.R., Sobel, E.R., McKnight, C.L., Schulein, B.J. & Wang, Z.X. (1992) Sedimentary record and climatic implications of recurrent deformation in the Tian-Shan — evidence from Mesozoic Strata of the North Tarim, South Junggar, and Turpan Basins, Northwest China. *Geol. Soc. Am. Bull.*, **104**(1), 53–79.

Hendrix, M.S., Dumitru, T. & Graham, S.A. (1994) Late Oligocene-early Miocene unroofing in the Chinese Tian-Shan: an early effect of the India-Asia collision. *Geology*, **22**(6), 487–490.

Herman, F., Seward, D., Valla, P.G., Carter, A., Kohn, B., Willett, S.D. & Ehlers, T.A. (2013) Worldwide acceleration of mountain erosion under a cooling climate. *Nature*, **504** (7480), 423–426.

Hidy, A.J., Gosse, J.C., Pederson, J.L., Mattern, J.P. & Finkel, R.C. (2010) A geologically constrained Monte Carlo approach to modeling exposure ages from profiles of cosmogenic nuclides: an example from Lees Ferry, Arizona. *Geochem. Geophys. Geosyst.*, **11**, 1–18.

Hooke, R.L. (1968) Steady-state relationships on arid-region alluvial fans in closed basins. *Am. J. Sci.*, **266**(8), 609–629.

Huntley, D.J., Godfrey-Smith, D.I. & Thewalt, M.L.W. (1985) Optical dating of sediments. *Nature*, **313**(5998), 105–107.

Jelinowska, A., Tucholka, P., Gasse, F. & Fontes, J.C. (1995) Mineral magnetic record of environment in Late Pleistocene and Holocene Sediments, Lake Manas, Xinjiang, China. *Geophys. Res. Lett.*, **22**(8), 953–956.

Jolivet, M., Dominguez, S., Charreau, J., Chen, Y., Li, Y. & Wang, Q. (2010) Mesozoic and cenozoic tectonic history of the central Chinese Tian Shan: reactivated tectonic structures and active deformation. *Tectonics*, **29**(6), 1–30.

Jolivet, M., Heilbronn, G., Robin, C., Barrier, L., Bourquin, S., Guo, Z., Jia, Y., Guerit, L., Yang, W. & Fu, B. (2013) Reconstructing the Late Palaeozoic — Mesozoic topographic evolution of the Chinese Tian Shan: available data and remaining uncertainties. *Adv. Geosci.*, **37**, 7–18.

Jolivet, M., Barrier, L., Dominguez, S., Guerit, L., Heilbronn, G. & Fu, B. (2014) Unbalanced sediment budgets in the catchment–alluvial fan system of the Kuitun River (northern Tian Shan, China): implications for mass-balance estimates, denudation and sedimentation rates in orogenic systems. *Geomorphology*, **214**, 168–182.

Kathayat, G., Cheng, H., Sinha, A., Spötl, C., Edwards, R.L., Zhang, H., Li, X., Yi, L., Ning, Y., Cai, Y., Lui, W.L. & Breitenbach, S.F.M. (2016) Indian monsoon variability on millennial-orbital timescales. *Sci. Rep.*, **6**, 24374–24378.

Lal, D. (1991) Cosmic-ray labeling of erosion surfaces –in situ nuclide production-rates and erosion models. *Earth Planet. Sci. Lett.*, **104**, 424–439.

Leopold, L.B. & Bull, W.B. (1979) Base level, aggradation, and grade. *Proc. Am. Philos. Soc.*, **123**, 168–202.

Li, C., Guo, Z. & Dupont-Nivet, G. (2010) Late Cenozoic tectonic deformation across the northern foreland of the Chinese Tian Shan. *J. Asian Earth Sci.*, **42**(5), 1–8.

Liu, Y., Métivier, F., Gaillardet, J., Ye, B., Meunier, P., Narteau, C., Lajeunesse, E., Han, T. & Malverti, L. (2011) Erosion rates deduced from seasonal mass balance along the upper Urumqi River in Tianshan. *Solid Earth*, **2**(2), 283–301.

Lu, H., Burbank, D.W. & Li, Y. (2010a) Alluvial sequence in the north piedmont of the Chinese Tian Shan over the past 550 kyr and its relationship to climate change. *Palaeogeogr. Palaeoclimatol. Palaeoecol.*, **285**(3–4), 343–353.

Lu, H., Burbank, D.W., Li, Y. & Liu, Y. (2010b) Late Cenozoic structural and stratigraphic evolution of the northern Chinese Tian Shan foreland. *Basin Res.*, **22**(3), 249–269.

Lu, H., Zhang, W., Li, Y., Dong, C., Zhang, T., Zhou, Z. & Zheng, X. (2013) Rock magnetic properties and paleoenvironmental implications of an 8-Ma Late Cenozoic terrigenous succession from the northern Tian Shan foreland basin, northwestern China. *Global Planet. Change*, **111**, 43–56.

Lu, H., Zhang, T., Zhao, J., Si, S., Wang, H., Chen, S. & Zheng, X. (2014) Late Quaternary alluvial sequence and uplift-driven incision of the Urumqi River in the north front of the Tian Shan, northwestern China. *Geomorphology*, **219**, 141–151.

Mackin, J.H. (1948) Concept of the Graded River. *Geol. Soc. Am. Bull.*, **59**(5), 463–511.

Malatesta, L.C., Prancevic, J.P. & Avouac, J.-P. (2017) Autogenic entrenchment patterns and terraces due to coupling with lateral erosion in incising alluvial channels. *J. Geophys. Res., series F*, **122**(1), 335–355.

Métivier, F. (2002) On the use of sedimentation rates in deciphering global change. *Geophys. Res. Lett.*, **29**(15), 41-1–41-4.

Métivier, F. & Gaudemer, Y. (1997) Mass transfer between eastern Tien Shan and adjacent basins (central Asia): constraints on regional tectonics and topography. *Geophys. J. Int.*, **128**(1), 1–17.

Métivier, F. & Gaudemer, Y. (1999) Stability of output fluxes of large rivers in South and East Asia during the last 2 million years: implications on floodplain processes. *Basin Res.*, **11**(4), 293–303.

Molnar, P. & England, P.C. (1990) Late Cenozoic uplift of mountain-ranges and global climate change – chicken or egg. *Nature*, **346**(6279), 29–34.

Molnar, P., Brown, E.T., Burchfiel, B.C., Qidong, D., Xianyue, F., Jun, L., Raisbeck, G., Sianbang, S., Zhangming, W., Yiou, F. & Huichuan, Y. (1994) Quaternary climate-change and the formation of river terraces across growing anticlines on the north flank of the Tien-Shan, China. *J. Geol.*, **102**(5), 583–602.

Nagashima, K., Tada, R., Tani, A., Sun, Y., Isozaki, Y., Toyoda, S. & Hasegawa, H. (2011) Millennial-scale oscillations of the westerly jet path during the last glacial period. *J. Asian Earth Sci.*, **40**(6), 1214–1220.

Neudorf, C.M., Roberts, R.G. & Jacobs, Z. (2012) Sources of overdispersion in a K-rich feldpar sample from north-central India: insights from, K content and IRSL age distributions for individual grains. *Radiat. Meas.*, **47**(9), 696–702.

Nian, X., Bailey, R.M. & Zhou, L. (2012) Investigations of the post-IR IRSL protocol applied to single K-feldspar grains from fluvial sediment samples. *Radiat. Meas.*, **47**, 703–709.

Nicholas, A.P. & Quine, T.A. (2007) Modeling alluvial landform change in the absence of external environmental forcing. *Geology*, **35**(6), 527–530.

Paola, C., Heller, P.L. & Angevine, C.L. (1992) The large-scale dynamics of grain-size variation in alluvial basins, 1: theory. *Basin Res.*, **4**(2), 73–90.

Parker, G., Paola, C., Whipple, K.X. & Mohrig, D. (1998a) Alluvial fans formed by channelized fluvial and sheet flow. I: theory. *J. Hydraul. Eng.*, **124**(10), 985.

Parker, G., Paola, C., Whipple, K.X., Mohrig, D., Toro-Escobar, C.M., Halverson, M. & Skoglund, T.W. (1998b) Alluvial fans formed by channelized fluvial and sheet flow. II: application. *J. Hydraul. Eng.*, **124**(10), 996.

Pepin, E., Carretier, S. & Herail, G. (2010) Erosion dynamics modelling in a coupled catchment-fan system with constant external forcing. *Geomorphology*, **122**, 78–90.

Poisson, B. (2002) Impact du climat et de la tectonique sur l'évolution géomorphologique d'un piémont: exemple du piémont Nord du Tian Shan depuis la fin du Pléistocène. PhD Thesis, Université Paris XI.

Poisson, B. & Avouac, J.-P. (2004) Holocene hydrological changes inferred from alluvial stream entrenchment in North Tian Shan (Northwestern China). *J. Geol.*, **112**(2), 231–249.

Puchol, N., Charreau, J., Blard, P.-H., Lavé, J., Dominguez, S., Pik, R., Saint-Carlier, D. & Team, A. (2016) Limited impact of Quaternary glaciations on denudation rates in Central Asia. *Geol. Soc. Am. Bull.*, **129**(3–4), 479–499.

Reigber, C., Michel, G.W., Galas, R., Angermann, D., Klotz, J., Chen, J.Y., Papschev, A., Arslanov, R., Tzurkov, V.E. & Ishanov, M.C. (2001) New space geodetic constraints on the distribution of deformation in Central Asia. *Earth Planet. Sci. Lett.*, **191**(1–2), 157–165.

Reimann, T., Thomsen, K.J., Jain, M., Murray, A.S. & Frechen, M. (2012) Single-grain dating of young sediments using the pIRIR signal from feldspar. *Quat. Geochronol.*, **11**, 28–41.

Rhodes, E.J. (2011) Optically stimulated luminescence dating of sediments over the past 200,000 years. *Annu. Rev. Earth Planet. Sci.*, **39**(1), 461–488.

Rhodes, E.J. (2015) Dating sediments using potassium feldspar single-grain IRSL: initial methodological considerations. *Quatern. Int.*, **362**, 14–22.

Rhodes, T.E., Gasse, F., Lin, R., Fontes, J.-C., Wei, K., Bertrand, P., Gibert, E., Mélières, F., Tucholka, P., Wang, Z. & Cheng, Z.-Y. (1996) A late Pleistocene-Holocene lacustrine record from Lake Manas, Zunggar (northern Xinjiang, western China). *Palaeogeogr. Palaeoclimatol. Palaeoecol.*, **120** (1–2), 105–121.

Rohais, S., Bonnet, S. & Eschard, R. (2012) Sedimentary record of tectonic and climatic erosional perturbations in an experimental coupled catchment-fan system. *Basin Res.*, **24** (2), 198–212.

Romans, B.W., Castelltort, S., Covault, J.A. & Fildani, A. (2015) Environmental signal propagation in sedimentary systems across timescales. *Earth Sci. Rev.*, **153**, 7–29.

Saint-Carlier, D., Charreau, J., Lavé, J., Blard, P.-H., Dominguez, S., Avouac, J.-P. & Wang, S. (2016) Major temporal variations in shortening rate absorbed along a large active fold of the southeastern Tianshan piedmont (China). *Earth Planet. Sci. Lett.*, **434**, 333–348.

Schneider, T., Bischoff, T. & Haug, G.H. (2014) Migrations and dynamics of the intertropical convergence zone. *Nature*, **513**(7516), 45–53.

Schumm, S.A. (1973) Geomorphic thresholds and complex response of drainage systems. In: *Fluvial Geomorphology* (Ed. by M. Morisawa), pp. 299–310. State University of New York, Binghamton, NY.

Simpson, G. & Castelltort, S. (2012) Model shows that rivers transmit high-frequency climate cycles to the sedimentary record. *Geology*, **40**, 1–4.

SMEDLEY, R.K., DULLER, G.A.T., PEARCE, N.J.G. & ROBERTS, H.M. (2012) Determining the K-content of single-grains of feldspar for luminescence dating. *Radiat. Meas.*, **47**(9), 790–796.

SMITH, G.S. & FERGUSON, R.I. (1996) The gravel-sand transition: flume study of channel response to reduced slope. *Geomorphology*, **16**, 147–159.

SOBEL, E.R. & DUMITRU, T.A. (1997) Thrusting and exhumation around the margins of the western Tarim basin during the India-Asia collision. *J. Geophys. Res.*, **102**(B3), 5043–5063.

SORG, A., BOLCH, T., STOFFEL, M., SOLOMINA, O. & BENISTON, M. (2012) Climate change impacts on glaciers and runoff in Tien Shan (Central Asia). *Nat. Clim. Chang.*, **2**(10), 725–731.

STOCKMEYER, J.M., SHAW, J.H. & GUAN, S. (2014) Seismic Hazards of Multisegment Thrust-Fault Ruptures: insights from the 1906 Mw 7.4-8.2 Manas, China, Earthquake. *Seismol. Res. Lett.*, **85**(4), 801–808.

STOCKMEYER, J.M., SHAW, J.H., BROWN, N.D., RHODES, E.J., RICHARDSON, P.W., WANG, M., LAVIN, L.C. & GUAN, S. (2017) Active thrust sheet deformation over multiple rupture cycles: a quantitative basis for relating terrace folds to fault slip rates. *Geol. Soc. Am. Bull.*, **129**(9–10), 1337–1356.

STROEVEN, A.P., HÄTTESTRAND, C., HEYMAN, J., KLEMAN, J. & MORÉN, B.M. (2013) Glacial geomorphology of the Tian Shan. *J Maps*, **9**(4), 505–512.

TAKEUCHI, N., FUJITA, K., AIZEN, V.B., NARAMA, C., YUSUKE, Y., OKAMOTO, S., NAOKI, K. & KUBOTA, J. (2014) The disappearance of glaciers in the Tien Shan Mountains in Central Asia at the end of Pleistocene. *Quatern. Sci. Rev.*, **103(C)**, 26–33.

TAPPONNIER, P. & MOLNAR, P. (1979) Active faulting and Cenozoic tectonics of the Tien Shan, Mongolia and Baykal regions. *J. Geophys. Res.*, **84**(NB7), 3425–3459.

THIEL, C., BUYLAERT, J.-P., MURRAY, A., TERHORST, B., HOFER, I., TSUKAMOTO, S. & FRECHEN, M. (2011) Luminescence dating of the Stratzing loess profile (Austria) – testing the potential of an elevated temperature post-IR IRSL protocol. *Quatern. Int.*, **234**(1–2), 23–31.

THOMPSON, S.C., ABDRAKHMATOV, K., WELDON, R., RUBIN, C.M., MOLNAR, P. & BERGER, G.W. (2002) Late Quaternary slip rates across the central Tien Shan, Kyrgyzstan, central Asia. *J. Geophys. Res.*, **107**(B9), ETG 7-1–ETG 7-32.

TRAUERSTEIN, M., LOWICK, S.E., PREUSSER, F. & SCHLUNEGGER, F. (2014) Small aliquot and single grain IRSL and post-IR IRSL dating of fluvial and alluvial sediments from the Pativilca valley, Peru. *Quat. Geochronol.*, **22**, 163–174.

TUCKER, G.E. & SLINGERLAND, R. (1997) Drainage basin responses to climate change. *Water Resour. Res.*, **33**(8), 2031–2047.

TUROWSKI, J.M., RICKENMANN, D. & DADSON, S.J. (2010) The partitioning of the total sediment load of a river into suspended load and bedload: a review of empirical data. *Sedimentology*, **57**(4), 1126–1146.

VAKS, A., GUTAREVA, O.S., BREITENBACH, S.F.M., AVIRMED, E., MASON, A.J., THOMAS, A.L., OSINZEV, A.V., KONONOV, A.M. & HENDERSON, G.M. (2013) Speleothems reveal 500,000-year history of Siberian permafrost. *Science*, **340**(6129), 183–186.

VANDENBERGHE, J., RENSSEN, H., van HUISSTEDEN, K., NUGTEREN, G., KONERT, M., LU, H., DODONOV, A. & BUYLAERT, J.-P. (2006) Penetration of Atlantic westerly winds into Central and East Asia. *Quatern. Sci. Rev.*, **25**, 2380–2389.

WANG, Y.J., CHENG, H., EDWARDS, R.L., AN, Z.S., WU, J.Y., SHEN, C.C. & DORALE, J.A. (2001) A high-resolution absolute-dated late Pleistocene Monsoon record from Hulu Cave, China. *Science*, **294**(5550), 2345–2348.

WANG, C.-Y., YANG, Z.-E., LUO, H. & MOONEY, W. (2004) Crustal structure of the northern margin of the eastern Tien Shan, China, and its tectonic implications for the 1906 M˜7.7 Manas earthquake. *Earth Planet. Sci. Lett.*, **223**(1–2), 187–202.

WANG, Y., CHENG, H., EDWARDS, R.L., KONG, X., SHAO, X., CHEN, S., WU, J., JIANG, X., WANG, X. & AN, Z. (2008) Millennial- and orbital-scale changes in the East Asian monsoon over the past 224,000 years. *Nature*, **451**(7182), 1090–1093.

WINDLEY, B.F., ALLEN, M., ZHANG, C., ZHAO, Z. & WANG, G.R. (1990) Palaeozoic accretion and Cenozoic redeformation of the Chinese Tien Shan Range, central Asia. *Geology*, **18**(2), 128–131.

WOLFF, C., PLESSEN, B., DUDASHVILLI, A.S., BREITENBACH, S.F., CHENG, H., EDWARDS, L.R. & STRECKER, M.R. (2016) Precipitation evolution of Central Asia during the last 5000 years. *The Holocene*, **27**(1), 142–154.

WOLMAN, M.G. (1954) A method of sampling coarse river-bed material. *Trans. Am. Geophys. Union*, **35**, 951–956.

YANG, X.-P., LI, A. & HUNAG, W. (2013) Uplift differential of active fold zones during the late Quaternary, northern piedmonts of the Tianshan Mountains, China. *Sci. China Earth Sci.*, **56**(794), 1–12.

YU, G., HARRISON, S.P. & XUE, B. (2001) Lake status records from China: Data Base Documentation. Technical Report 4, Max Planck Institute für Biogeochemie, Jena, Germany.

ZHANG, P.Z., MOLNAR, P. & DOWNS, W.R. (2001) Increased sedimentation rates and grain sizes 2-4 Myr ago due to the influence of climate change on erosion rates. *Nature*, **410**(6831), 891–897.

Manuscript received 14 March 2017; In revised form 27 September 2017; Manuscript accepted 6 October 2017.